JACS
JOURNAL OF THE AMERICAN CHEMICAL SOCIETY
Article
pubs.acs.org/JACS

Consequences of Surface Oxophilicity of Ni, Ni-Co, and Co Clusters on Methane Activation

Weifeng Tu,[†] Mireille Ghoussoub,[‡] Chandra Veer Singh,*[,‡,§] and Ya-Huei Cathy Chin*[,†]

[†]Department of Chemical Engineering and Applied Chemistry, University of Toronto, Toronto, Ontario M5S 3E5, Canada
[‡]Department of Materials Science and Engineering, University of Toronto, Toronto, Ontario M5S 3E4, Canada
[§]Department of Mechanical and Industrial Engineering, University of Toronto, Toronto, Ontario M5S 3G8, Canada

Supporting Information

ABSTRACT: This study describes a new C−H bond activation pathway during CH_4−CO_2 reactions on oxophilic Ni-Co and Co clusters, unlike those established previously on Ni clusters. The initial C−H bond activation remains as the sole kinetically relevant step on Ni-Co, Ni, and Co clusters, but their specific reaction paths vary. On Ni clusters, C−H bond activation occurs via an oxidative addition step that involves a three-center $(H_3C\cdots*\cdots H)^{‡}$ transition state, during which a Ni-atom inserts into the C−H bond and donates its electron density into the C−H bond's antibonding orbital. Ni-Co clusters are more oxophilic than Ni; thus, their surfaces are covered with oxygen adatoms. An oxygen adatom and a vicinal Co-atom form a metal−oxygen site-pair that cleaves the C−H bond via a σ bond metathesis reaction, during which the Co inserts into the C−H bond while the oxygen abstracts the leaving H-atom in a concerted, four-center $(H_3C\cdots*\cdots H\cdots O*)^{‡}$ transition state. Similarly, Co clusters also catalyze the σ bond metathesis step, but much less effectively because of their higher oxophilicities, much stronger binding to oxygen, and less effective hydrogen abstraction than Ni-Co clusters. On Ni-Co and Co clusters, the pseudo-first-order rate coefficients are single-valued functions of the CO_2-to-CO ratio (or H_2O-to-H_2 ratio), because this ratio prescribes the oxygen chemical potentials and the relative abundances of metal−oxygen site-pairs through the water−gas shift equilibrium. The direct involvement of reactive oxygen in the kinetically relevant step leads to more effective CH_4 turnovers and complete elimination of coke deposition on Ni-Co bimetallic clusters.

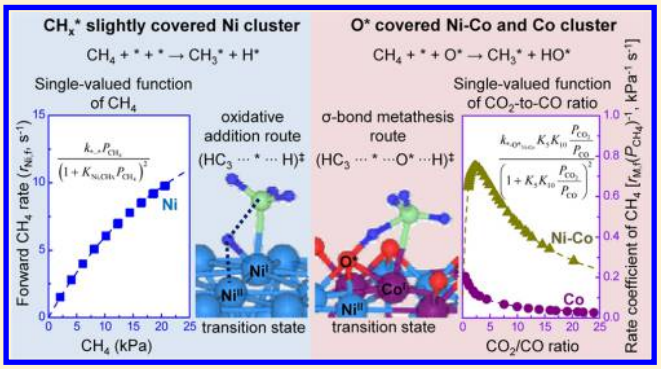

1. INTRODUCTION

Reaction of methane and carbon dioxide is an attractive route for producing a CO−H_2 mixture as a chemical precursor for commodity chemical and liquid fuel synthesis. The reaction involves an initial methane activation on transition metals [clusters: Ni,[1−3] Pd,[3,4] Pt,[3,5] Rh,[3,6−9] Ir,[3,10,11] and Ru;[3,12] surfaces: Ni(111),[13−17] Rh(111),[18] Ru(1120),[19] and Co(111)[20]] and transition metal complexes [$Au(HSO_4)_3$,[21] Pt^{II}-NHC (N-heterocyclic carbenes),[22] Pd^0-NHC,[23] Pd-$(PH_3)_2$,[24] and (η^5-phospholyl)$Rh(CO)_2$[25]], examined extensively with rate and isotopic assessments,[1,4,5,9−12] spectroscopic studies,[2,6−8] and first-principle density functional theory (DFT) calculations.[13,14,17−20,22−24] On transition metal surfaces [Ni(111),[13−17] Rh(111),[18] Ru(1120),[19] Co(111),[20] and Pd clusters[26,27]], the initial methane activation is the kinetically relevant step, catalyzed by a metal atom via an oxidative addition pathway mechanistically analogous to those undergone by homogeneous catalytic complexes [$Au(HSO_4)_3$,[21] Pd^{II}-NHC,[23] and $Pd(PH_3)_2$[24]]. The oxidative addition step involves metal atom (*) insertion into the C−H bond via a late, three-center $(H_3C\cdots*\cdots H)^{‡}$ transition state, during which the metal atom donates its electron density into the C−H antibonding orbital (σ_{C-H}*).[27] C−H bond activation barriers relate closely to the extent of metal-to-CH_3 interactions at the $(H_3C\cdots*\cdots H)^{‡}$ transition state and, through the Brønsted−Evans−Polanyi relation, to the binding energies of CH_3 moieties on the surfaces.[27]

These previous studies have established the consensus that an increase in methane turnovers requires more effective C−H bond activation, attained when metal atoms bind more strongly to the CH_3 fragments at the transition state, thus reducing the activation enthalpy. The binding to CH_3 fragments, however, should not be too strong such that the metal sites remain free of carbon debris. Attempts to modify metal surfaces and their reactivities toward C−H bond activation have remained the subject of intense research. Incorporating a secondary element into the Ni clusters constitutes one of these attempts; the secondary element may decorate the cluster surfaces (Ni−B[15,28] and Ni−S[29]), incorporate as a surface alloy (Ni−Pt[30,31] and Ni−Sn[16,32]), or form a bulk alloy (Ni-Co[33]) with Ni. Such modifications (1) break the Ni site ensemble required for

Received: February 15, 2017
Published: April 17, 2017

DOI: 10.1021/jacs.7b01632
J. Am. Chem. Soc. XXXX, XXX, XXX−XXX

carbon nucleation and growth (B,[15,28] Sn,[16,32] and S[29]), (2) promote reducibility and thus retain metal clusters in their metallic state (by adding Pt to Ni[31]), (3) increase the overall dispersion (Ni−Pt[30] and Ni-Co[33]), and/or (4) alter the d-bandwidth and d-band center of the metal clusters [Au/Ni(211),[34] Cu/Ni(111),[35,36] Co/Ni(111),[13,36] or Fe/Ni(111)[36]] and, in turn, their interactions with reactive intermediates. In particular, the effects of alloy formation on the d-band levels and, in turn, on the C−H bond activation barrier of first-row transition metal and alloy surfaces have been examined extensively with DFT calculations.[13,34−37]

Despite the large number of studies, a clear connection between the structures of these bi-elemental clusters and their specific functions in C−H bond activation or in retarding coke deposition has not been unambiguously established. This is caused, in large part, by challenges in acquiring intrinsic rate data and in probing the actual catalytic structures at the working state, because (1) strong endothermicities lead to significant temperature and concentration gradients prevalent across catalyst pellets and reactor bed, (2) thermodynamic constraints limit the conversion, (3) bimetallic clusters may reconstruct and perhaps segregate (Fe-Ni[38,39]), and (4) carbon or oxygen may solvate into the cluster bulk, altering both the surface and bulk structures (Co[40]). On the other hand, DFT studies focus predominantly on pristine, uncovered surfaces [Ni(111),[14−17] Rh(111),[18] Ru(1120),[19] Co(111),[20] Au/Ni(211),[34] Cu/Ni(111),[35,36] Co/Ni(111),[13,36] or Fe/Ni(111)[36]]. These static, model structures of ideal surfaces with minimal flexibilities to reconstruct may not capture the dynamics and site evolvement of actual, working metal cluster surfaces.

In contrast to these previous studies and their associated mechanistic interpretations, we report and confirm here the dynamic, instantaneous evolvement of reactive oxygen adatoms, occurring when incorporating Co as a secondary oxophilic metal into Ni clusters or on monometallic Co clusters. These oxygen adatoms and their vicinal metal sites form metal−oxygen site-pairs that activate the C−H bond in methane through pathways mechanistically similar to those that prevail during CH_4−O_2 catalysis on PdO clusters[41] and on O*-covered Pt clusters,[42] despite the seemingly different chemical identities of oxidant (CO_2 vs O_2) and operating oxygen chemical potential ranges in dry reforming (CH_4−CO_2) and combustion (CH_4−O_2) reactions. The oxygen virtual pressures[43,44] at the active sites, which dictate the oxygen coverages during CH_4−CO_2 reactions, range from 10^{-19} to 10^{-23} kPa (determined with CO_2-to-CO ratios between 1 and 100, $CO_2 \leftrightarrow CO + 0.5O_2$) at 873 K. These values are at least 19 orders of magnitude lower than those during CH_4−O_2 reactions, at 1−100 kPa O_2. We show that the metal−oxygen sites emerge only *in situ* and incipiently on oxophilic surfaces, making their detection and characterizations difficult. These metal−oxygen sites catalyze C−H bond activation via a σ bond metathesis route that leads to CH_3 and H moieties bound to the metal atom and the chemisorbed oxygen, respectively, and to activation enthalpies and entropies unlike those of the oxidative addition route. Their kinetic significance leads the first-order rate coefficients on Ni-Co clusters and monometallic Co clusters to depend strictly on the operating CO_2-to-CO ratio, because the CO_2-to-CO ratio determines the oxygen chemical potentials and thus the abundances of metal−oxygen site-pairs on these clusters. The combination of a reactive oxygen and a metal atom on the Ni-Co clusters results in more effective C−H bond activation than that on Ni or Co monometallic clusters, because (1) the σ bond metathesis pathway is more effective than the oxidative addition pathway, providing that a weakly bound and highly reactive oxygen involves in abstracting the leaving H-atom during the C−H bond activation, (2) weakly bound oxygen adatoms on Ni-Co surfaces are more basic than those on Co surfaces, and thus they are more effective in abstracting the leaving H-atom, and (3) oxygen adatoms on Ni-Co clusters effectively oxidize and remove the carbonaceous intermediates during CH_4−CO_2 reactions, leading to cluster surfaces largely free of carbonaceous debris, thus keeping the active sites unoccupied and available for C−H bond activation.

2. METHODS

2.1. Synthesis of Supported Ni, Co, and Ni-Co Clusters on MgO−ZrO_2 Catalysts. MgO−ZrO_2 supports (MgO:ZrO_2 molar ratio of 5:2) were prepared by co-precipitation method. Stoichiometric quantities of $Mg(NO_3)_2{\cdot}6H_2O$ (Sigma-Aldrich, 99.999% trace metals basis) and $ZrO(NO_3)_2{\cdot}6H_2O$ (Sigma-Aldrich, 99% trace metals basis) were dissolved in doubly deionized water (>18.2 MΩ·cm, 0.5 dm^3, 0.70 M Mg^{2+} and 0.28 M ZrO^{2+}) under constant stirring at 333 ± 2 K. An aqueous ammonium carbonate solution [2 M $(NH_4)_2CO_3$, Sigma-Aldrich, ACS reagent] was added dropwise (0.03 cm^3 s^{-1}) to the mixture at 333 ± 2 K, such that the pH was maintained at 9.5 ± 0.5 throughout the co-precipitation step. The solution was then cooled to ambient temperature, and the precipitates were separated by filtration (Fisher brand filter paper, coarse porosity, particle retention >20 μm). The solid samples [$Mg(OH)_2$-$ZrO(OH)_2$] were treated in ambient air at 393 K for 24 h and then at 1073 K (0.05 K s^{-1}) for 5 h.

Catalysts with either 12 g-atom% Ni or 12 g-atom% Co clusters supported on MgO−ZrO_2 (denoted as 12Ni/MgO−ZrO_2 or 12Co/MgO−ZrO_2, respectively; g-atom% equals molar fraction) were synthesized by impregnating the MgO−ZrO_2 powders with an aqueous solution (2 cm^3 solution per gram of MgO−ZrO_2), prepared by dissolving the respective precursor [$Ni(NO_3)_2{\cdot}6H_2O$ (Sigma-Aldrich, 99.999% trace metals basis) or $Co(NO_3)_2{\cdot}6H_2O$ (Sigma-Aldrich, 99.999% trace metals basis)] in deionized water (>18.2 MΩ·cm). Bimetallic catalysts with 6 g-atom% Ni and 6 g-atom% Co supported on MgO−ZrO_2 (denoted as 6Ni-6Co/MgO−ZrO_2) were prepared by impregnating MgO−ZrO_2 powders with an aqueous solution of $Ni(NO_3)_2{\cdot}6H_2O$ and $Co(NO_3)_2{\cdot}6H_2O$ dissolved in deionized water [>18.2 MΩ·cm, 2 cm^3 solution (gram of MgO−ZrO_2)$^{-1}$]. After the impregnation, these samples were heat-treated at 393 K for 24 h in ambient air, followed by heating in flowing 5% H_2/Ar (Linde certified standard, 5.22%, 1 cm^3 g^{-1} s^{-1}) at 0.05 K s^{-1} to 1023 K and holding isothermally at 1023 K for 2 h. These catalyst powders were diluted with ZrO_2 powders (Sigma-Aldrich, 99% trace metals basis, 0−5 μm particle size) to form well-mixed physical mixtures at ZrO_2-to-catalyst intraparticle dilution ratios between 5 and 40. The physical mixtures were subsequently pressed into pellets and sieved to retain 125−180 μm agglomerates.

2.2. Isothermal H_2 Uptakes, Quantification of Oxygen and Carbon Contents, and Determination of the Bulk Chemical State of Metal Clusters. The average metal cluster diameters were determined from irreversible H_2 uptakes at 313 K, measured with volumetric adsorption techniques. The catalyst samples were first treated *in situ* under flowing 5% H_2/Ar (Linde certified standard, 5.22%, 1 cm^3 g^{-1} s^{-1}) by heating from ambient temperature to 1023 K at 0.05 K s^{-1} and holding for 2 h at 1023 K. The samples were then evacuated under dynamic vacuum at 1023 K for 1 h and cooled under dynamic vacuum to 313 K for the isothermal H_2 uptake measurements. H_2 uptakes were measured at 313 K between 0 and 14 kPa H_2; two hydrogen uptake isotherms were measured consecutively, and between these measurements, the sample was evacuated under dynamic vacuum at 313 K for 0.5 h. The fraction of surface metal atoms was determined from the difference between the extrapolated values from the two isotherms to zero H_2 pressures, by assuming an atomic stoichiometry for H-to-surface metal of unity (H/M_s = 1,

DOI: 10.1021/jacs.7b01632
J. Am. Chem. Soc. XXXX, XXX, XXX−XXX

where M_s denotes surface metal atom). The average cluster diameters were estimated from these dispersion values by assuming hemispherical clusters with densities similar to those of bulk Ni, Co, and Ni-Co alloy of 8.901, 8.900, and 8.901 g cm^{-3} (the average between Ni and Co), respectively.[43]

The chemical state of metal clusters when in contact with a CO_2−CO mixture or O_2 was determined by mass changes in thermogravimetric analysis (SENSYS EVO TG-DSC, S60/58129). Catalyst samples (20 mg, 12Co/MgO−ZrO_2 or 6Ni-6Co/MgO−ZrO_2) were treated in the microbalance under flowing 5% H_2/Ar (Linde certified standard, 5.22%, 41 cm^3 g^{-1} s^{-1}) at a constant heating rate of 0.17 K s^{-1} to 1023 K, held for 2 h, and then cooled to 873 K in flowing Ar (Linde, 99.9993%, 41 cm^3 g^{-1} s^{-1}), followed by evacuating under dynamic vacuum at 873 K for 1 h. The pretreated sample was exposed to 10 kPa Ar (Linde, 99.9993%, 9.1 cm^3 g^{-1} s^{-1}) at 873 K for 600 s, and then 40 kPa CO_2−CO−Ar gas mixture (9.1 cm^3 g^{-1} s^{-1}), prepared from mixing CO_2 (Linde, 99.99%) and CO/Ar (Linde certified standard, 5.25% CO/Ar) at CO_2-to-CO ratios of 20 ± 0.5 or 32 ± 0.5, at 873 K for 4 h. The inlet and outlet of the microbalance were sealed when the absolute pressure of the gas mixture reached 50 kPa. In a separate experiment, the pretreated sample was exposed to 45 kPa Ar (Linde, 99.9993%, 9.1 cm^3 g^{-1} s^{-1}) and then to 5 kPa O_2 (Linde, 99.99%, 9.1 cm^3 g^{-1} s^{-1}) for 4 h, during which the oxygen uptakes were measured. The mass changes of these samples throughout these processes were measured with the microbalance operating under batch mode in a closed system at 873 K. The oxygen uptakes were determined from the mass changes and normalized with either the number of surface metal sites (M_s) or the number of total metal atoms (M_t) of the sample. These uptake values reflect the total oxygen contents of the clusters at these different CO_2-to-CO ratios or 5 kPa O_2.

The amount of carbon-containing debris on the catalyst samples formed upon their exposure to CO_2−CO mixtures (CO_2-to-CO ratios of 20, 9.1 cm^3 g^{-1} s^{-1}, 873 K, 4 h) or CH_4−CO_2 mixtures (5−20 kPa CH_4, 10 kPa CO_2, balance Ar, 48−638 cm^3 g^{-1} s^{-1}, 873 K, 300 s) was determined by oxygen titration carried out with a microcatalytic plug flow reactor system at 873 K. The carbon quantification was carried out after removing the CO_2−CO or CH_4−CO_2 mixture and purging the sample under flowing Ar (1.67 cm^3 s^{-1}) at 873 K for 1 h. After these treatments, 0.5% O_2/Ar [Linde certified standard, 2.2 × 10^{-8} mol (O_2) s^{-1}] was introduced to the samples at 873 K. The carbon contents were related to the total amount of CO_2 and CO produced from the oxygen reactions with the carbon-containing species. The CO_2 and CO formed were converted to CH_4 in a methanator and then quantified with an online gas chromatograph (Agilent 7890A) equipped with a flame ionization detector without the need for separation.

2.3. Rates of CH_4 Conversion and Reverse Water−Gas Shift Reactions, Approaches to Chemical Equilibrium, and CH_4/CD_4 Kinetic Isotopic Effects during Steady-State CH_4−CO_2 Reactions. The catalyst and ZrO_2 agglomerates (125−180 μm) were physically mixed with SiO_2 (Sigma-Aldrich, quartz sand, acid purified, 125−180 μm) at a SiO_2-to-catalyst bed dilution ratio between 20 and 100. The agglomerates and SiO_2 mixtures were held on a quartz supporting frit to form a packed catalyst bed in a tubular microcatalytic plug flow reactor (8.1 mm reactor i.d.) equipped with a K-type thermocouple placed at the center (in both axial and radial directions) of the packed bed. All samples were treated *in situ* under flowing 5% H_2/Ar (Linde certified standard, 5.22%, 166−277 cm^3 g^{-1} s^{-1}) at a constant heating rate of 0.05 K s^{-1} to 1023 K, held for 2 h, and then cooled to reaction temperatures (773−1023 K) in flowing Ar (Linde, 99.9993%, 166−277 cm^3 g^{-1} s^{-1}) before exposure to CH_4−CO_2 reactants. Reactant mixtures were prepared from metering 47% CH_4/Ar (Linde certified standard), CO_2 (Linde, 99.99%), and Ar (Linde, 99.9993%) independently with thermal mass flow controllers (Brooks, SLA5850). The effects of H_2, CO, or H_2O products on CH_4 reforming rates were measured by incorporating H_2 (Linde, 99.999%), 5.25% CO/Ar (Linde certified standard), or H_2O(g) into the flowing CH_4−CO_2−Ar reactant stream. H_2O(g) was introduced by evaporating deionized liquid H_2O, fed into a vaporization zone through a gastight syringe (0.25 cm^3, Hamilton) mounted on a syringe infusion pump (KD Scientific, LEGATO 100), in which it was mixed with the reactant stream at 383 K. All transfer gas lines were heated to 400 K after H_2O introduction to prevent water condensation. Water was removed from the gas stream by a water trap containing Drierite with indicators (Sigma-Aldrich, 98% $CaSO_4$ and 2% $CoCl_2$; 1−4 mm particle size) before entering a micro gas chromatograph (Varian CP-4900) for reactant and product (CH_4, CO_2, CO, and H_2) quantifications. The micro gas chromatograph was equipped with HP-PLOT U and Mol Sieve 5A columns connected to thermal conductivity detectors.

C−H/C−D kinetic isotopic effects were measured with CH_4−CO_2 and CD_4-CO_2 mixtures at 873 K using the microcatalytic plug flow reactor system described above. CD_4 was prepared by complete conversion of CO_2 (Linde, 99.99%) and D_2 (Linde, 99.995%, isotopic contents of 99.7%) on 12Ni/MgO−ZrO_2 via methanation reactions at 473 K in a separate reactor. CD_4 was identified and quantified with an online gas chromatograph (Agilent 7890A)-mass spectrometer (Agilent 5975C), GC-MS, equipped with HP-5 capillary column (Agilent, 19091J-413, 30 m, 0.32 mm i.d., 0.25 μm film) connected to a mass selective detector. Concentrations of CD_4, CO, CO_2, and D_2 from CD_4−CO_2 reactions were quantified with the micro gas chromatograph (Varian CP-4900).

2.4. Density Functional Theory (DFT) Calculations of C−H Bond Activation of Methane on Ni(111), Oxygen-Covered Co(111), and Oxygen-Covered Ni-Co(111) Surfaces. All structure and energy calculations were performed via periodic plane-wave DFT calculations using the Vienna ab initio simulation package (VASP). A 64-atom, 4×4×4 supercell, with ∼20 Å vacuum was used to model the Ni(111), Co(111), and Ni-Co(111) surfaces. The (111) surface was chosen, as it is the most thermodynamically stable surface of Ni and Co with face-centered cubic (fcc) crystallographic structure over the temperature range of the reaction (773−1023 K).[45] Computation was performed using the Perdew−Burke−Ernzerhof (PBE) exchange correlation functional,[46] together with the projector augmented-wave (PAW) method-based pseudo-potentials.[47,48] Kinetic energy cutoffs and the self-consistent field convergence criterion were set to 400 eV and 10^{-4} eV, respectively. Brillouin zone integrations were performed with 4×4×1 Monkhorst−Pack k-point mesh.[49] Wave function occupancies were determined using the second-order Methfessel−Paxton smearing over a width of 0.2 eV. All calculations were spin-polarized to account for the magnetic properties of Ni and Co. Within the four-layer slab, the atoms from the bottom two layers were frozen in all calculations after an initial geometric optimization of the bulk structure, while the atoms from the top two layers, gas-phase species, and adsorbed species were allowed to relax. Relaxation was performed using the conjugate gradient minimization algorithm until the energy difference between ionic steps was $<10^{-3}$ eV. The enthalpy of adsorption (ΔE_{ads}) was defined by

$$\Delta E_{ads} = E_{adsorbate/surface} - (E_{adsorbate} + E_{surface}) \quad (1a)$$

where $E_{adsorbate/surface}$ is the total energy of the surface containing the adsorbed species, and the ($E_{adsorbate}$ + $E_{surface}$) term is the total energy of the free adsorbate (in the gas phase at non-interacting distance) and bare metal surfaces. By this definition, negative adsorption enthalpies indicate exothermic adsorption. To develop a model for the bimetallic Ni-Co surfaces, the effect of Co clustering at the surfaces of a bimetallic Ni-Co crystal was investigated by computing the cohesive energies of six surfaces in which the location of secondary Co-atoms among the Ni-atoms was randomly generated using a MATLAB code. In each model, the bottom two layers were composed of Ni-atoms that were frozen, while the top two layers contained a 3:1 Ni-to-Co ratio with randomly distributed Co-atoms, and all the atoms in the top two layers were free to move under relaxation calculations. The structures were relaxed to their minimum energy, and no significant change in cohesive energy was found among the different structures. Therefore, the Ni-Co(111) surface with 1:1 Ni-to-Co atomic ratio with alternating Ni- and Co-atom rows was chosen to represent the miscible alloy surfaces. The enthalpies for the adsorption of a single oxygen adatom at 1/16 ML O* (herein and after ML denotes

DOI: 10.1021/jacs.7b01632
J. Am. Chem. Soc. XXXX, XXX, XXX−XXX

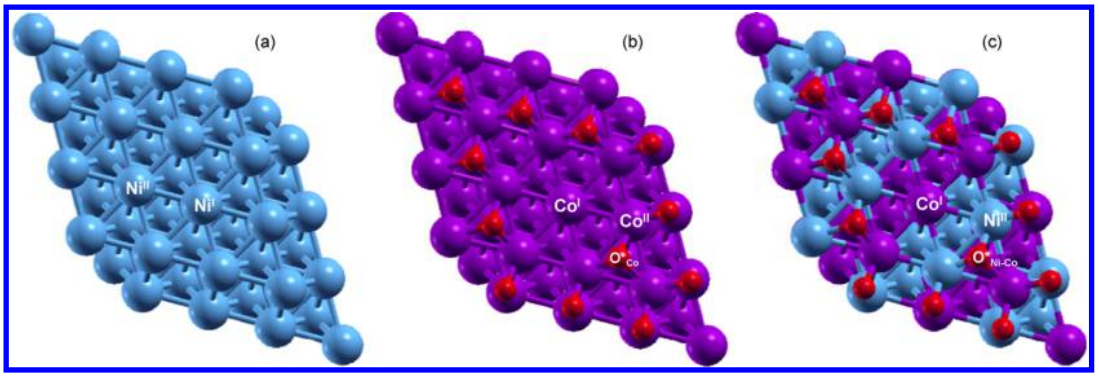

Figure 1. Top view of slab models used in DFT calculations: (a) Ni(111) surface, (b) 0.75 ML O*-covered Co(111) surface, and (c) 0.75 ML O*-covered Ni-Co(111) surface. Blue represents Ni-atoms, purple represents Co-atoms, and red represents O-atoms. Ni^{I}–Ni^{II} refers to Ni metal atom site-pair (*-*) on Ni(111), Co^{I}–O^{*}_{Co} denotes the metal–oxygen site-pair (*-O^{*}_{Co}) on 0.75 ML O*/Co(111), and Co^{I}–$O^{*}_{Ni\text{-}Co}$ denotes the metal–oxygen site-pair (*-$O^{*}_{Ni\text{-}Co}$) on 0.75 ML O*/Ni-Co(111) surfaces.

monolayer) were calculated for all possible adsorption sites on the bare Ni(111), Co(111), or Ni-Co(111) surfaces. Their values were found to be greatest at hexagonal close-packed (hcp) sites compared to those at atop sites and fcc sites. Given these findings, 0.75 ML O*-covered Co(111) and Ni-Co(111) models were generated with oxygen bound to the hcp sites, as shown in Figure 1. The O* binding energy (E_{BE}) was defined as the reaction energy required to remove an O*-atom on an O*-covered (111) surface to a non-interacting distance:

$$E_{BE} = E_{nO^*/surface} - (E_{(n-1)O^*/surface} + E_O) \quad (1b)$$

where $E_{nO^*/surface}$ and $E_{(n-1)O^*/surface}$ are the total energy of the surfaces containing n and $n-1$ chemisorbed oxygen adatoms on O*-covered (111) surface, respectively, and E_O is the energy of an oxygen radical. The term ($E_{(n-1)O^*/surface} + E_O$) was calculated by removing the oxygen from the surfaces to a non-interacting distance.

The structures and energies of the reactant, transition, and product states in the activation of C–H bond in CH_4 were investigated on a Ni metal atom site-pair (*-*) (labeled as Ni^{I}–Ni^{II} in Figure 1a) on Ni(111) surface, a Co-atom and oxygen site-pair (*-O^{*}_{Co}) (labeled as Co^{I}–O^{*}_{Co} in Figure 1b) on 0.75 ML O*/Co(111), and Co-atom and oxygen site-pair (*-O^{*}_{Ni-Co}) (labeled as Co^{I}–$O^{*}_{Ni\text{-}Co}$ in Figure 1c) on 0.75 ML O*/Ni-Co(111) surfaces. Transition states and activation barriers along a minimum energy reaction path were determined using the climbing image nudged elastic-band (CI-NEB) method[50] with 10 images. Bader charge analysis[51,52] was used to obtain the relative charges associated with individual atoms at the reactant state, transition state, and product state for C–H bond activation on Ni(111), O*-covered Co(111), and O*-covered Ni-Co(111) surfaces.

3. RESULTS AND DISCUSSION

3.1. First-Order Rate Coefficients of Methane Are a Single-Valued Function of CH_4 Pressure on Ni Clusters and of CO_2-to-CO ratio on Co and Ni-Co Alloy Clusters, Because These Parameters Dictate the Carbon and Oxygen Chemical Potentials, Respectively, at the Cluster Surfaces. We measured the rate and selectivity data in the regime of strict kinetic control, attained by extensive site dilutions and confirmed with Koros–Nowak criterion[53] that rates (per site) remain independent of reactor volume, heat loads, and a further increase in the intraparticle and catalyst bed dilution ratios to values above 5 and 50, respectively. Next, measured CH_4 conversions and selectivities remained independent of time and within experimental errors (±5%) during the entire duration of rate measurements (>100 h, Figure S2). Thus, surface reconstruction, carbon deposition, and sintering of metal clusters did not occur during the time scale of rate measurements. Last, CH_4 conversions were lower than 14% in all rate measurements. These conversions, after correcting for the approach to chemical equilibrium, give the forward CH_4 conversion rates. Section S1 of the Supporting Information provides the details and experimental evidence that led to these conclusions. Thus, all rate and selectivity data reported herein reflect intrinsic catalytic events at cluster surfaces, free of corruptions arising from transport gradients, site reconstruction and poisoning, and thermodynamics.

Forward rates of methane conversion ($r_{M,f}$, per surface metal site; subscript M denotes Ni, Co, or Ni-Co clusters, respectively, and subscript f denotes the forward rate) for CH_4–CO_2 reactions were measured over a broad range of CH_4 (2–25 kPa), CO_2 (2–40 kPa), H_2O (0.1–5 kPa), H_2 (0.3–10 kPa), and CO (0.7–6 kPa) pressures on Ni (26 nm), Co (30 nm), and Ni-Co (27 nm) clusters at 873 K. First-order rate coefficients ($k^{1st}_{M,f}$, M = Ni, Co, or Ni-Co) are defined as the forward methane turnover rates ($r_{M,f}$) divided by CH_4 pressure (P_{CH_4}). The rate coefficients acquire distinct dependencies [α_M and β_M (or β'_M)], depending on the metal identity (M = Ni, Co, Ni-Co):

$$k^{1st}_{M,f} = \frac{r_{M,f}}{P_{CH_4}} = k_{app,M}(P_{CH_4})^{\alpha_M}\left(\frac{P_{CO_2}}{P_{CO}}\right)^{\beta_M} = k'_{app,M}(P_{CH_4})^{\alpha_M}\left(\frac{P_{H_2O}}{P_{H_2}}\right)^{\beta'_M} \quad (2)$$

$k_{app,M}$ and $k'_{app,M}$ are the apparent rate constants; α_M is the apparent dependence on CH_4 pressure; β_M is the apparent dependence on the CO_2-to-CO pressure ratio, P_{CO_2}/P_{CO}, and β'_M is that on the H_2O-to-H_2 pressure ratio, P_{H_2O}/P_{H_2}. The first-order rate coefficients for Ni clusters (12Ni/MgO–ZrO_2), $k^{1st}_{Ni,f}$, decreased slightly with increasing CH_4 pressure (α_{Ni} = −0.1 ± 0.05). At each CH_4 pressure, they remained independent of CO_2-to-CO ratios (P_{CO_2}/P_{CO} = 2.5–20) or H_2O-to-H_2 ratios (P_{H_2O}/P_{H_2} = 0.4–3.6); thus, β_{Ni} and β'_{Ni} values are near zero (~0 ± 0.05), as shown in Figure 2a. In contrast, these rate coefficients on Co clusters ($k^{1st}_{Co,f}$) and Ni-Co bimetallic clusters ($k^{1st}_{Ni\text{-}Co,f}$) exhibited different trends; they were both independent of CH_4 pressure (α_{Co} = 0 ± 0.05 and $\alpha_{Ni\text{-}Co}$ = 0 ± 0.05) and a single-valued function of the CO_2-to-CO or H_2O-to-H_2 ratios, irrespective of the individual reactant (2–25 kPa CH_4 and 4–40 kPa CO_2) and product (0.3–10 kPa H_2, 0.7–6 kPa CO, and 0.1–5 kPa H_2O) pressures, as captured

DOI: 10.1021/jacs.7b01632
J. Am. Chem. Soc. XXXX, XXX, XXX–XXX

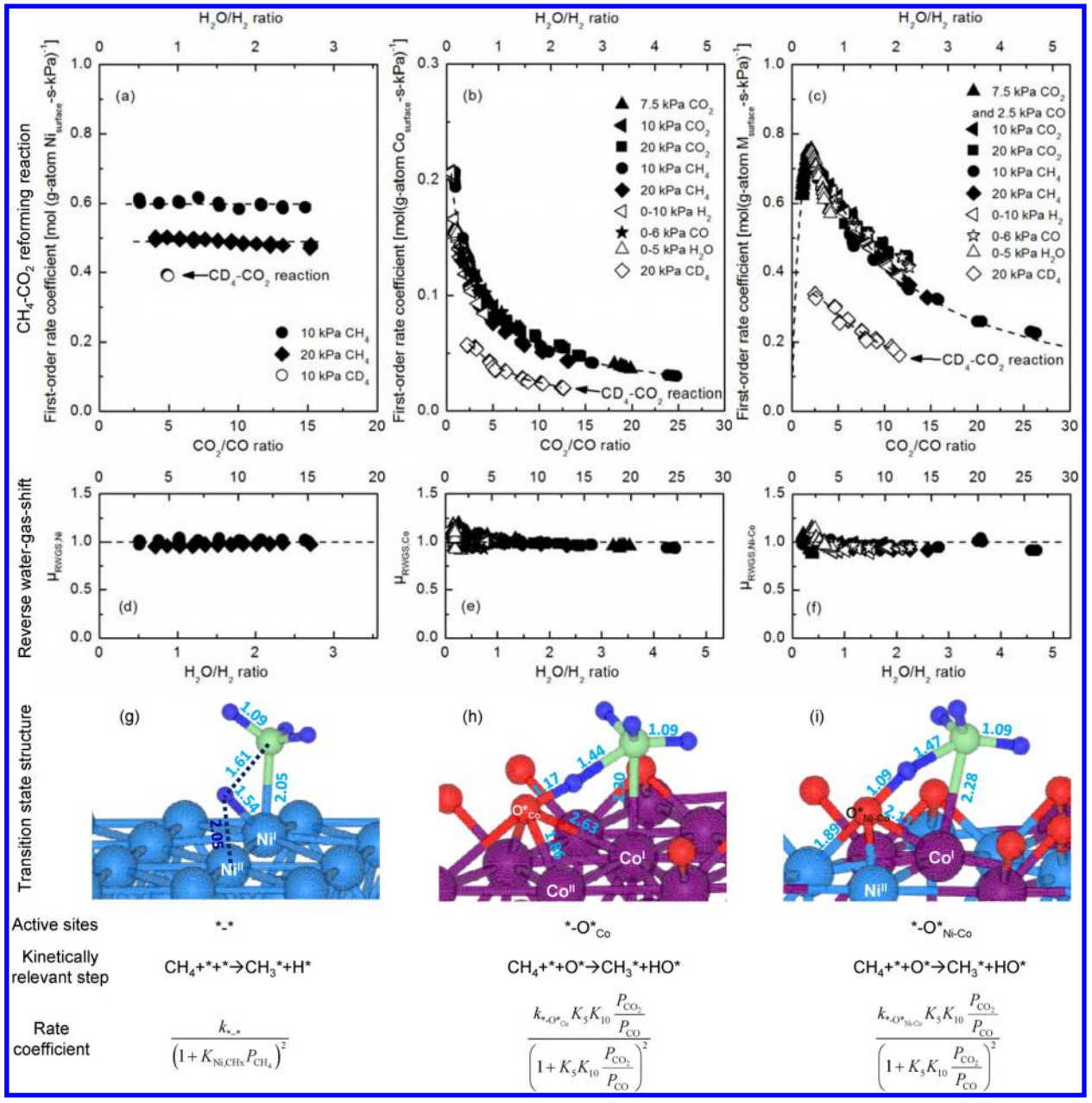

Figure 2. First-order rate coefficients [(a–c), $k^{1st}_{M,f}$, subscript M = Ni, Co, or Ni-Co; (---) in (a-c): predicted values from regression of rate data with eqs 6, 10, and 12, respectively] of CH_4 forward conversion and the approach-to-equilibrium values [(d–f), $\mu_{RWGS,M}$, eq S4] for reverse water–gas shift reactions as single-valued functions of CO_2-to-CO ratio or H_2O-to-H_2 ratio during CH_4–CO_2 reactions at 873 K on Ni [(a,d), 12Ni/MgO–ZrO_2, 26 nm], Co [(b,e), 12Co/MgO–ZrO_2, 30 nm], and Ni-Co [(c,f), 6Ni-6Co/MgO–ZrO_2, 27 nm] clusters (10 ZrO_2-to-catalyst intraparticle dilution and 90 SiO_2-to-catalyst bed dilution; 4.60×10^5–3.45×10^6 $cm^3\ g_{cat}^{-1}\ h^{-1}$). Structure and bond distance (bond distance unit in Å) of transition state (g–i) for the initial C–H bond dissociation in CH_4 catalyzed by a *-* site-pair on Ni(111) surface (g), a *-O^*_{Co} site-pair on 0.75 ML O*/Co(111) surface (h), and a *-$O^*_{Ni\text{-}Co}$ site-pair on 0.75 ML O*/Ni-Co(111) surface (i); active site-pairs, kinetically relevant steps, and first-order rate coefficients (eqs 6, 10, and 12) on Ni, Co, and Ni-Co clusters ($k_{*\text{-}*}$, $k_{*\text{-}O^*_{Co}}$, $k_{*\text{-}O^*_{Ni\text{-}Co}}$, K_{Ni,CH_x}, K_5, and K_{10} are defined in Table 1).

in Figure 2b,c with the CO_2-to-CO or H_2O-to-H_2 ratios plotted as the primary and secondary x-axes, respectively. The rate coefficients on Co clusters ($k^{1st}_{Co,f}$) decreased as the CO_2-to-CO or H_2O-to-H_2 ratios increased ($\beta_{Co} = -0.55 \pm 0.20$; $\beta'_{Co} = -0.52 \pm 0.20$; Figure 2b) over the entire range of pressure ratios. The rate coefficients on Ni-Co bimetallic clusters ($k^{1st}_{Ni\text{-}Co,f}$) exhibited a bimodal, volcano-type dependence (Figure 2c): their values increased as the CO_2-to-CO ratio ($\beta_{Ni\text{-}Co} = 0.70 \pm 0.10$) increased from 1.1 to 2.0, but decreased as the ratio exceeded 2.0 ($\beta_{Ni\text{-}Co} = -0.50 \pm 0.30$). These trends with the CO_2-to-CO ratios are similar to those with the H_2O-to-H_2 ratios, as captured in Figure 2b,c, confirming that these ratios must be inter-related. The specific functional dependencies [α_M and β_M (or β'_M), in Table S1] differ among the metals, because of the distinct kinetically relevant steps, active site structures, and most abundant surface intermediates, caused predominantly by the difference in surface oxophilicity and thus the extent of oxygen involvement in the kinetically relevant step, as confirmed in Sections 3.2–3.4.

The reverse water–gas shift reaction (RWGS, eq S1c in the Supporting Information), which occurs concomitantly with the CH_4–CO_2 reactions, is chemically equilibrated on all three

DOI: 10.1021/jacs.7b01632
J. Am. Chem. Soc. XXXX, XXX, XXX–XXX

catalysts, as its approach-to-equilibrium values ($\mu_{RWGS,M}$, M = Ni, Co, or Ni-Co) equal unity (1.0 ± 0.2) over the entire operating range (Figure 2d–f). Thus, CO_2-to-CO (P_{CO_2}/P_{CO}) and H_2O-to-H_2 (P_{H_2O}/P_{H_2}) pressure ratios relate to each other through the thermodynamic relationship

$$\frac{P_{CO_2}}{P_{CO}} = \frac{1}{K_{RWGS}}\frac{P_{H_2O}}{P_{H_2}} \quad (3)$$

where K_{RWGS} is the equilibrium constant for the RWGS reaction (eq S1c). The chemical equilibrium suggests that CO_2 activation steps and steps associated with H_2, CO, and H_2O formation must remain equilibrated and therefore kinetically irrelevant, as also reported for Ni/MgO,[1] Rh/Al_2O_3,[9] Pt/ZrO_2,[5] and Ir/ZrO_2[10,11] catalysts during CH_4–CO_2 and CH_4–H_2O reactions.

Table 1. Generalized Catalytic Sequence and Elementary Steps for CH_4–CO_2 Reactions on Ni, Co, and Ni-Co Clusters[a]

	kinetically relevant step	rate and equilibrium constant
1a	$CH_4 + * + * \rightarrow CH_3* + H*$	$k_{*,*}$ on Ni clusters
1b[b]	$CH_4 + * + O* \rightarrow CH_3* + OH*$	$k_{*\text{-}O*_{Co}}$ on Co clusters
		$k_{*\text{-}O*_{Ni\text{-}Co}}$ on Ni-Co clusters
	other steps on Ni, Co, Ni-Co clusters	
2	$CH_3* + * \rightarrow CH_2* + H*$	k_2
3	$CH_2* + * \rightarrow CH* + H*$	k_3
4	$CH* + O* \rightarrow HCO* + *$	k_4
4a	$CH* + * \rightarrow C* + H*$	k_{4a}
5	$CO_2 + * + * \leftrightarrow CO* + O*$	K_5
6	$HCO* + * \rightleftharpoons CO* + H*$	$k_{6,f}$, $k_{6,r}$
6a	$C* + O* \rightleftharpoons CO* + *$	$k_{6a,f}$, $k_{6a,r}$
7	$H* + O* \leftrightarrow OH* + *$	K_7
8	$OH* + OH* \leftrightarrow H_2O + * + O*$	K_8
9	$H* + H* \leftrightarrow H_2 + * + *$	K_9
10	$CO* \leftrightarrow CO + *$	K_{10}
11	$O_2(v) + * + * \leftrightarrow O* + O*$	K_{11}

[a]Key to symbols: *, an unoccupied metal site; →, an irreversible step; ↔, a quasi-equilibrated step; and ⇌, a reversible step. $O_2(v)$ denotes oxygen virtual pressure [b]Step 1b occurs on Co and Ni-Co clusters covered with reactive oxygen species.

Table 1 shows a proposed, generalized sequence of elementary steps that captures the unique dependencies of the first-order rate coefficients ($k^{1st}_{M,f}$, M = Ni, Co, or Ni-Co) on the operating CH_4 pressures or CO_2-to-CO ratios; the latter also relate to H_2O-to-H_2 ratios (eq 3) in Figure 2a–c. This catalytic sequence contains all dominant steps required for CO_2 and H_2O reforming and the RWGS reaction. Despite their similarities, the identities of the kinetically relevant step and of the active site-pair differ among the Ni, Co, and Ni-Co bimetallic clusters. Specifically, active site-pairs for the initial, kinetically relevant C–H bond activation vary from the strict involvement of Ni-atom site-pair (*-*) on Ni clusters, to Co- and O-atom site-pair (*-$O*_{Co}$) on Co clusters, to the Co- and O-atom site-pair (*-$O*_{Ni-Co}$) on Ni-Co bimetallic clusters. Within this catalytic sequence, the RWGS equilibrium requires that CO_2-to-CO ratios and the related H_2O-to-H_2 ratios (through eq 3) dictate the oxygen chemical potential at cluster surfaces and thus the surface density of reactive oxygen adatoms.

The surface density of oxygen, defined here as the oxygen-to-unoccupied metal site ratio, [O*]-to-[*], is as follows (derivation in Section S2 of the Supporting Information):

$$\frac{[O*]}{[*]} = K_5K_{10}\frac{P_{CO_2}}{P_{CO}} = \frac{K_9}{K_7{}^2K_8}\frac{P_{H_2O}}{P_{H_2}} = K_{11}{}^{0.5}\left(\frac{P_{O_2(v)}}{P^{\ominus}}\right)^{0.5} \quad (4)$$

where equilibrium constants K_5, K_7, K_8, K_9, K_{10}, and K_{11} are defined in Table 1, $P^{\ominus}$ refers to the standard atmosphere. As shown in eq 4, the [O*]-to-[*] site ratio directly reflects the oxygen virtual pressure ($P_{O_2(v)}$), a fictitious oxygen pressure that is in equilibrium with the surface O* and thus a rigorous surrogate of the oxygen coverages (through Step 11, Table 1) and the thermodynamic activity of oxygen at cluster surfaces during steady-state catalysis.[44,54–56] Not only do the oxygen virtual pressure ($P_{O_2(v)}$) and the related CO_2-to-CO and H_2O-to-H_2 ratios determine the surface oxygen contents, they also dictate the thermodynamically stable phase of these clusters during steady-state catalysis.

In what follows, we interpret these unique dependencies in Figure 2 with mechanism-based rate equations and kinetic parameters, confirming the proposed molecular events, active site structures, and their kinetic relevance with rate and isotopic studies, oxygen uptake/titration, and DFT calculations. We begin with reactions on monometallic Ni, monometallic Co, and then bimetallic Ni-Co clusters in Sections 3.2, 3.3, and 3.4, respectively. We focus on describing how the different types of active site-pairs, namely *-*, *-$O*_{Co}$, and *-$O*_{Ni-Co}$, begin to evolve on Ni, Co, and Ni-Co clusters, respectively, their different catalytic functions during the kinetically relevant C–H bond activation, and the resulting marked differences in activation barriers and entropies. Finally, we relate these events to the observed catalytic dependence and discuss their implications in designing more effective catalysts for C–H bond activation and improving the resistance toward coke deposition.

3.2. Kinetically Relevant C–H Bond Activation Catalyzed by Ni Metal Site-Pair (*-*) on Monometallic Ni Clusters Partially Covered with Reactive Carbonaceous Intermediates.

Figure 3 shows the effects of CH_4 (2–25 kPa, panel a), CO_2 (5–40 kPa, panel b), and reaction products [H_2 (0.3–10 kPa), CO (0.7–6 kPa), and H_2O (0.1–5 kPa); panel c] on the forward CH_4 conversion rates ($r_{Ni,f}$, per surface Ni-atom) during CH_4–CO_2 reactions on monometallic Ni clusters at 873 K. The forward rates increased less than linearly with increasing CH_4 pressure (Figure 3a) and remained insensitive to the pressures of co-reactant (CO_2) and products (H_2, CO, and H_2O). This dependence is nearly identical to the strict first-order dependence on CH_4 pressure, reported previously on smaller, monometallic Ni, Rh, Pt, and Ir clusters (6.8 nm Ni,[1,16] 4.0 nm Rh,[9] 6.3 nm Pt,[5] and 1.9 nm Ir[10,11]) at similar conditions (CH_4-to-CO_2 ratio = 0.2–1.5 at 873 K;[1,5,9–11] CH_4-to-H_2O ratio = 0.4–1.6 for 1013–1073 K[16]). The slight deviation from the linear relation may indicate site occupation by methane-derived intermediates (CH_x*, x = 0–4), which reduces the fraction of available Ni sites for CH_4 activation.[16,28,32] Titration of the CH_x* debris after steady-state CH_4–CO_2 reactions in 5, 10, and 20 kPa CH_4 and 10 kPa CO_2 by CH_x* reaction with oxygen gave the carbon coverages. The carbon coverages, defined here as the molar ratios of CH_x to surface Ni (CH_x*/Ni_s), increased from 0.15 to 0.27 as the CH_4 pressure increased from 5 to 20 kPa during CH_4–CO_2

DOI: 10.1021/jacs.7b01632
J. Am. Chem. Soc. XXXX, XXX, XXX–XXX

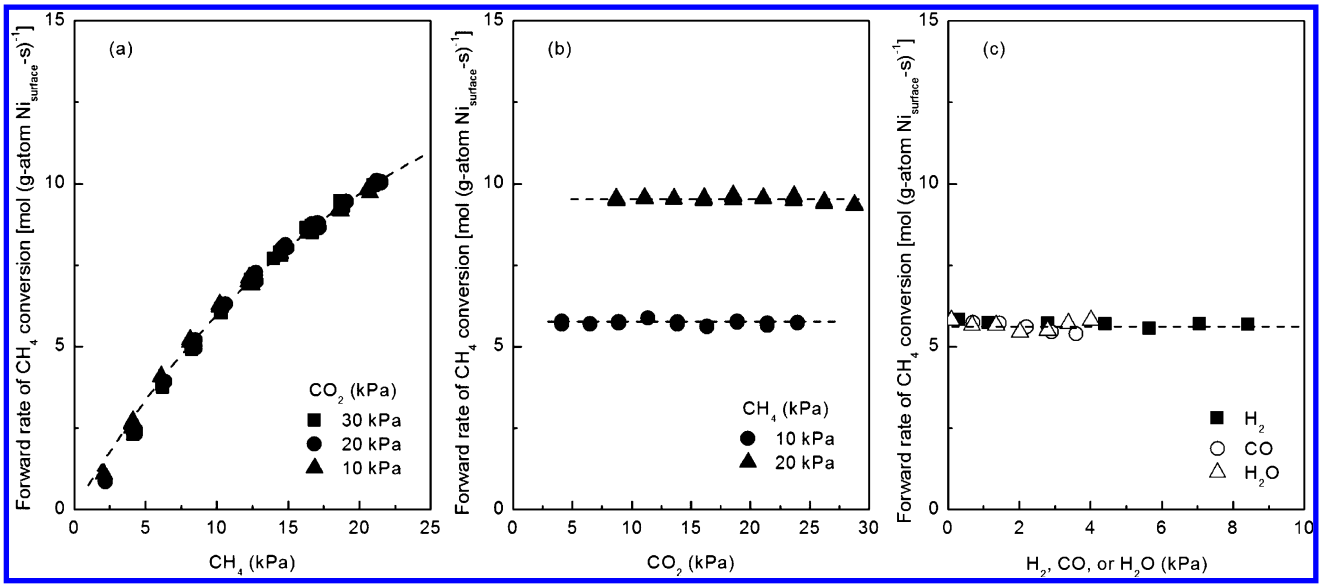

Figure 3. Effects of CH_4 (a), CO_2 (b), and product [(c); 10 kPa CH_4−10 kPa CO_2 with 0.3−10 kPa H_2 (■), 0.7−6 kPa CO (●), or 0.1−5 kPa H_2O (▲)] pressures on CH_4 forward conversion rate [$r_{Ni,f}$, per surface Ni-atom; (---): predicted CH_4 forward rate from regression of rate data with eq 5] during CH_4−CO_2 reactions at 873 K on 12Ni/MgO−ZrO_2 (12 g-atom% Ni dispersed on MgO−ZrO_2) (3 mg of catalyst, 26 nm mean Ni cluster diameter, 10 ZrO_2-to-catalyst intraparticle dilution and 90 SiO_2-to-catalyst bed dilution; 2.3×10^6 cm^3 g_{cat}^{-1} h^{-1}).

reactions at 873 K, as shown in Figure 4. These ratios, together with rates that increase less than linearly with CH_4 pressures, confirm that Ni cluster surfaces must be partially covered with CH_4-derived species.

These rate dependencies shown in Figure 3a−c suggest that CH_4 activation is a kinetically relevant step, occurred at the vacant sites on Ni clusters, on which CH_4-derived intermediates (CH_x*, x = 0−4) occupy a small portion of the sites. We note that both dry and wet reforming reactions occur concomitantly and the activation of CH_4, not of the co-reactants, limits rates, because rates remain insensitive to CO_2 and H_2O pressures. Mechanistically, CH_4 first dissociates irreversibly on a Ni-atom site-pair, forming a CH_3* species and a chemisorbed H* (Step 1a, Table 1). The CH_3* species dissociates in a series of irreversible C−H bond cleavage steps that leads to CH* (Steps 2 and 3). The CH* recombines with an atomic O*, forming a formyl intermediate (HCO*, Step 4) that undergoes the last C−H bond activation (Step 6) to form CO* and H*, which desorb as CO (Step 10) and, upon recombination with another H*, as H_2 (Step 9), respectively. We propose that the first C−H bond activation is an irreversible, kinetically relevant step for CH_4−CO_2 reactions on Ni clusters, consistent with the energies determined from DFT calculations for CH_4 decomposition on Ni(111) surfaces[16,17] and with kinetic and isotopic evidence on Ni clusters.[1,16] CO_2 activation (Step 5, Table 1), H_2 desorption (Step 9), CO desorption (Step 10), and H_2O formation (Steps 7 and 8), which include all steps required for the RWGS reaction, are quasi-equilibrated, as described in Section 3.1. The assumption of the initial C−H bond dissociation in CH_4 as the kinetically relevant step (Step 1a) and applying pseudo-steady-state hypotheses on all intermediates in Table 1 lead to the rate equation for forward CH_4 turnovers ($r_{Ni,f}$, derivation in Section S3 of the Supporting Information):

$$r_{Ni,f} = \frac{k_{*-*}P_{CH_4}}{(1 + K_{Ni,CH_x}P_{CH_4})^2} \quad (5)$$

where k_{*-*} is the rate constant for the first C−H bond activation on Ni-atom site-pairs (*-*, Step 1a) and the K_{Ni,CH_x} term reflects the coverage of carbon debris, likely at the minority, unsaturated corner and edge sites. Nonlinear regression of eq 5 against all rate data in Figure 3, by minimizing the sum of squared residuals, gives the values of these rate and equilibrium

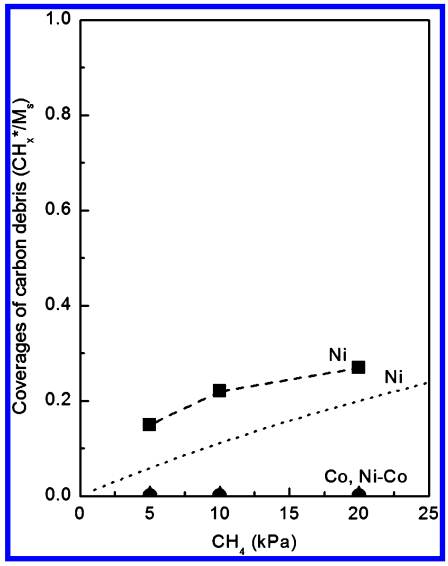

Figure 4. Effects of CH_4 pressure on the coverages of carbon containing debris [expressed in terms of the ratio of CH_x* fragment (CH_x*) to surface metal site (M_s, M = Ni, Co, or Ni-Co), CH_x*/M_s] on Ni, Co, and Ni-Co clusters during CH_4−CO_2 reactions at 873 K [Ni clusters (■), 12Ni/MgO−ZrO_2, 26 nm; Co clusters (●), 12Co/MgO−ZrO_2, 30 nm; Ni-Co bimetallic clusters (▲), 6Ni-6Co/MgO−ZrO_2, 27 nm; 10 ZrO_2-to-catalyst intraparticle dilution and 90 SiO_2-to-catalyst bed dilution; 4.60×10^5−3.45×10^6 cm^3 g_{cat}^{-1} h^{-1}; (■, ●, and ▲), measured by titrating the CH_x* fragments with oxygen pulses after exposure of the sample to CH_4−CO_2 mixtures; (···), predicted by eq 5 with the equilibrium constant of carbon debris formation on Ni clusters, K_{M,CH_x}, given in Table 2].

DOI: 10.1021/jacs.7b01632
J. Am. Chem. Soc. XXXX, XXX, XXX−XXX

Table 2. Rate Parameters of CH_4 Forward Conversion during CH_4-CO_2 Reactions on Ni, Co, and Ni-Co Clusters at 873 K[a]

catalyst	rate equation	k_{*-*}	$k_{*-O^*_{Co}}$	$k_{*-O^*_{Ni-Co}}$	K_{M,CH_x}	K_5K_{10}
		[mol (g-atom $M_{surface}$-s-kPa)$^{-1}$]			[kPa^{-1}]	[unitless]
12Ni/MgO−ZrO_2	$\frac{k_{*-*}P_{CH_4}}{(1+K_{Ni,CH_x}P_{CH_4})^2}$	0.76 ± 0.06			0.013 ± 0.002	
12Co/MgO−ZrO_2	$\frac{k_{*-O^*_{Co}}K_5K_{10}P_{CH_4}\frac{P_{CO_2}}{P_{CO}}}{\left(1+K_5K_{10}\frac{P_{CO_2}}{P_{CO_2}}\right)^2}$		0.51 ± 0.06			0.72 ± 0.05
6Ni-6Co/MgO−ZrO_2	$\frac{k_{*-O^*_{Ni-Co}}K_5K_{10}P_{CH_4}\frac{P_{CO_2}}{P_{CO}}}{\left(1+K_5K_{10}\frac{P_{CO_2}}{P_{CO}}\right)^2}$			3.0 ± 0.15		0.42 ± 0.04

[a] k_{*-*}, $k_{*-O^*_{Co}}$, and $k_{*-O^*_{Ni-Co}}$ are the rate constants of C−H bond activation of CH_4 on Ni, O*-covered Co, and O*-covered Ni-Co clusters, respectively; K_5 and K_{10} are the equilibrium constants for Steps 5 and 10 in Table 1, respectively; K_{M,CH_x} reflects the carbon debris coverages at the unsaturated corner and edge sites.

Table 3. Active Sites, Measured C−H/C−D Kinetic Isotope Effects (KIEs), Measured Activation Barriers and Entropies, and DFT-Calculated Activation Barriers for C−H Bond Activation in CH_4 on Ni, O*-Covered Co, and O*-Covered Ni-Co Clusters and Closed-Packed (111) Surfaces[a]

catalyst	active sites	C−H/C−D KIE, $k_{i,C-H}/k_{i,C-D}$ (at 873 K)	activation barrier, $E_{a,i}$ [kJ mol^{-1}]	activation entropy, $\Delta S_i^{\ddagger}$ [J mol^{-1} K^{-1}]	DFT-calculated activation barrier, $E_{a,calc,i}$ [kJ mol^{-1}]
12Ni/MgO−ZrO_2 (26 nm)	*-*	1.49 ± 0.05	85 ± 10	−112 ± 10	75.4
12Co/MgO−ZrO_2 (30 nm)	*-O^*_{Co}	2.03 ± 0.10	148 ± 10	−41 ± 10	172 (0.75 ML O*)
6Ni-6Co/MgO−ZrO_2 (27 nm)	*-O^*_{Ni-Co}	2.15 ± 0.10	95 ± 10	−87 ± 10	132 (0.75 ML O*)

[a] Subscript i indicates the identity of active site-pair (i = *-*, *-O^*_{Co}, or *-O^*_{Ni-Co}, on Ni, O*-covered Co, or O*-covered Ni-Co clusters, respectively).

constants, as summarized in Table 2, with the parity plot for the measured and estimated rates shown in Figure S4. eq 5 together with the equilibrium constant value for K_{Ni,CH_x} gives the predicted carbon coverages (CH_x*/Ni_s ratios) during steady-state reactions at 873 K, as also included in Figure 4. The predicted CH_x*/Ni_s ratios increased from 0.06 to 0.20 as the CH_4 pressure increased from 5 to 20 kPa. These predicted ratios are slightly lower than the measured CH_x* coverages (0.15−0.27, Figure 4) titrated by oxygen, an indication that carbon species not only occupy the Ni sites but also remain on the MgO−ZrO_2 supports. The forward rates ($r_{Ni,f}$, eq 5), when divided by CH_4 pressure, give the first-order rate coefficients ($k^{1st}_{Ni,f}$):

$$k^{1st}_{Ni,f} = \frac{r_{Ni,f}}{P_{CH_4}} = \frac{k_{*-*}}{(1+K_{Ni,CH_x}P_{CH_4})^2} \quad (6)$$

Therefore, the rate coefficients are a single-valued function of CH_4 pressures and independent of CO_2-to-CO or H_2O-to-H_2 ratios, as depicted in Section 3.1 and shown in Figure 2a.

The kinetic relevance of the C−H bond activation step was confirmed from C−H/C−D kinetic isotope effects (KIEs), determined from the rate data obtained with 10 kPa CH_4−10 kPa CO_2 and 10 kPa CD_4−10 kPa CO_2 mixtures and shown in Figure 2a. The elementary rate constant ratio for the initial C−H bond to C−D bond activation [KIE = $k_{*-*,C-H}/k_{*-*,C-D}$] was determined by regressing the rate data in Figure 2a with eq 6 to be 1.49 (873 K, Table 3). This KIE of 1.49 is in agreement with those found on monometallic transition metal clusters (1.41 on Pd,[4] 1.42 on Ru,[12] 1.56 on Rh,[9] 1.62 on Ni,[1] 1.75 on Ir,[11] and 1.77 on Pt,[5] at 873 K).

Previous DFT calculations have shed light onto the stabilities of the various intermediates and transition states during sequential cleavages of the C−H bonds in CH_4 on Ni(111) surfaces.[16,17] From these studies, the calculated barrier, when referring to the reactant state of the specific step, is 87 kJ mol^{-1} for the first C−H bond activation of CH_4 (Step 1a). The barrier decreases to 67 kJ mol^{-1} for the second C−H bond activation (of CH_3*, Step 2) and then to 33 kJ mol^{-1} for the third C−H bond activation (of CH_2*, Step 3).[17] These relative barriers suggest that CH_4, upon its initial activation, decomposes via a series of rapid H-abstraction steps to CH*. The sequential recombination of CH* with O* (Step 4) that forms HCO* occurs with a barrier of 150 kJ mol^{-1} on single-crystal Ni(111) surfaces, and the consecutive activation of the HCO* that cleaves the last C−H bond (Step 6) occurs almost readily with a barrier below 20 kJ mol^{-1}.[14,57] In contrast, the alternative route of CH* dissociation (barrier: 135 kJ mol^{-1} and heat of reaction: 54 kJ mol^{-1} on Ni(111),[57] Step 4a) that forms C* and H* followed by the recombination of the C* with O* to produce CO* (barrier: 206 kJ mol^{-1} on Ni(111),[57] Step 6a) proceeds at a much larger overall barrier than the CH* oxidation route (via HCO*) [effective barrier: 260 kJ mol^{-1} for the CH* direct dissociation (Steps 4a and 6a) vs 150 kJ mol^{-1} for the CH* oxidation route (Steps 4 and 6)].[14,57] Thus, the CH* direct dissociation route (Step 4a) is unlikely to occur.[14,57] We stress that neither the O*−CH* (Step 4) nor O*−C* (Step 6a) recombination, both of which occur much later along the reaction coordinate than the initial C−H bond activation, is kinetically relevant, despite their higher activation barriers, because O* involvement in the kinetically relevant step would lead the rate to depend on oxygen coverages and, in

DOI: 10.1021/jacs.7b01632
J. Am. Chem. Soc. XXXX, XXX, XXX−XXX

Table 4. Bader Charges of H, CH_3, and Chemisorbed Oxygen (O^*_{Co} or $O^*_{Ni\text{-}Co}$) during C−H Bond Activation on Ni(111), 0.75 ML O*/Co(111), and 0.75 ML O*/Ni-Co(111) Surfaces at the Reactant State, Transition State, and Product State[a]

	reactant state			transition state			product state		
catalyst surface	H	CH_3	O	H	CH_3	O	H	CH_3	O
Ni(111)	0.05	−0.08		0.10	−0.18		0.06	−0.38	
0.75 ML O*/Co(111)	0.05	−0.06	−0.71	0.52	−0.16	−0.88	0.72	−0.10	−1.14
0.75 ML O*/Ni-Co(111)	0.05	−0.05	−0.69	0.58	−0.06	−0.99	0.72	−0.07	−1.10

[a]Negative values refer to higher electron density.

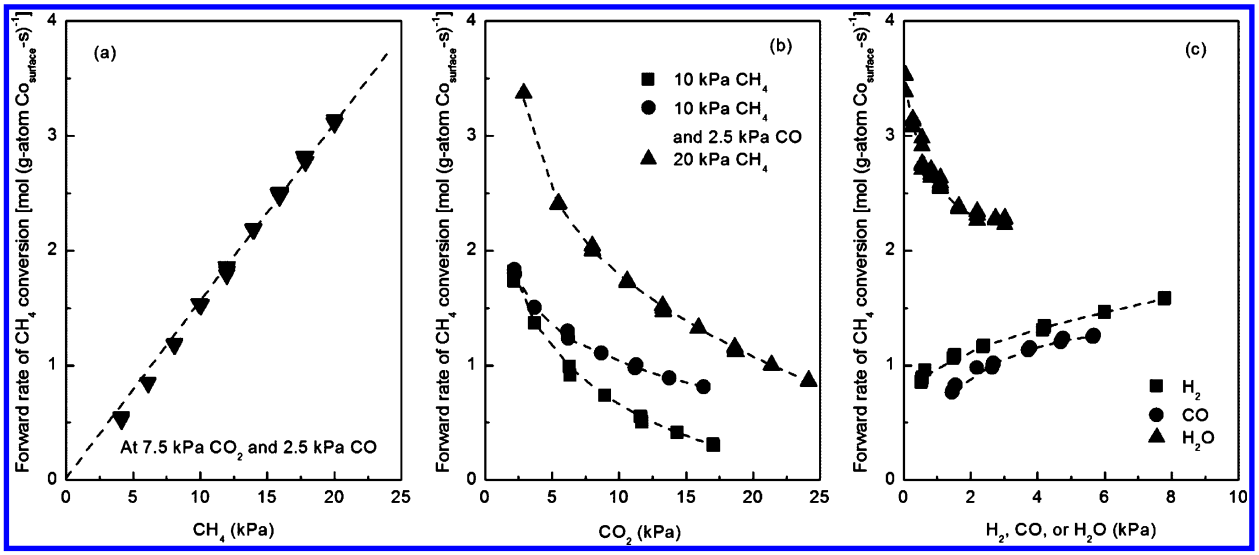

Figure 5. Effects of CH_4 (a), CO_2 (b), and product [(c); 10 kPa CH_4-10 kPa CO_2 with 0.5−10 kPa H_2 (■) or 1.5−6 kPa CO (●); 20 kPa CH_4-3 kPa CO_2 with 0.1−5 kPa H_2O (▲)] partial pressures on CH_4 forward conversion rate [$r_{Co,f}$, per surface Co-atom; (---): predicted CH_4 forward rate from regression of rate data with eq 9] during CH_4−CO_2 reactions at 873 K on 12Co/MgO−ZrO_2 (12 g-atom% Co dispersed on MgO−ZrO_2) (15 mg of catalyst, 30 nm mean Co cluster diameter, 10 ZrO_2-to-catalyst intraparticle dilution and 90 SiO_2-to-catalyst bed dilution; 4.6×10^5 cm^3 g_{cat}^{-1} h^{-1}).

turn, on the CO_2-to-CO ratios (as shown in eqs S20 and S22, Section S3 of the Supporting Information). The initial C−H bond activation remains kinetically relevant, because of its larger activation entropy losses required to evolve the C−H bond activation transition state, when comparing to those during O*−CH* (Step 4) or O*−C* (Step 6a) recombination.

DFT calculations on the initial, kinetically relevant C−H bond activation on Ni(111) facets show that this step proceeds via oxidative addition of a Ni-atom (labeled as Ni^I in Figure 2g) into the C−H bond, weakening and elongating it from 1.10 Å in CH_4(g) (Figure S5a) to 1.61 Å at the three-center carbon−metal-hydrogen $[H_3C\cdots*\cdots H]^{\ddagger}$ transition state (Figure 2g) with a barrier of 75.4 kJ mol^{-1} (Table 3). At the transition state, the C−Ni^I bond distance is 2.05 Å, H−Ni^I bond distance is 1.54 Å, and the distance between the leaving H-atom and the vicinal Ni site (labeled as Ni^{II} in Figure 2g) is 2.05 Å. This H−Ni^{II} distance is much longer than that of the product state at 1.72 Å (Figure S5c). These bond distances and the transition-state structure indicate that the vicinal Ni site (Ni^{II}) does not assist with the C−H bond activation, but instead promotes the H transfer later along the reaction coordinate. The Bader charge (Table 4) at CH_3 moieties decreases slightly (−0.10) at the transition state and becomes slightly more negative (−0.38) at the product state, suggesting that electron densities donate from Ni into the orbitals of the C−H bond. The Bader charge at the H species, however, does not appear to vary (<±0.05) along the entire reaction coordinate.

3.3. Kinetically Relevant C−H Bond Activation Catalyzed by Metal−Oxygen Site-Pair (*-O^*_{Co}) and Evidence for Near O* Surface Saturation during CH_4−CO_2 Reactions on Monometallic Co Clusters.

Next, we provide the experimental and theoretical evidence for the C−H bond activation pathway on Co clusters, distinctly different than that on Ni clusters. Co-atoms preferentially bind to chemisorbed oxygen (O*), because of their much higher oxophilicity than Ni: the binding energy for the most stable O* (eq 1b) on bare Co(111) is −550 kJ mol^{-1}, whereas that on bare Ni(111) is −496 kJ mol^{-1}.[58] These O* adatoms assist in C−H bond activation.

Figure 5 shows the dependence of forward methane turnover rates ($r_{Co,f}$, per surface Co-atom) on reactant (4−25 kPa CH_4 and 2−25 kPa CO_2) and product (0.5−10 kPa H_2, 1.5−6 kPa CO, and 0.1−5 kPa H_2O) pressures during CH_4−CO_2 reactions on Co clusters (30 nm) at 873 K. Similar to those on Ni clusters, the rates increased proportionally with CH_4 pressure (Figure 5a). These rates, however, decreased with increasing CO_2 and H_2O pressures (Figure 5b,c). The extent of CO_2 inhibition became smaller when CO (2.5 kPa) was added (Figure 5b). In fact, both CO (1.5−6 kPa) and H_2 (0.5−10 kPa) addition promoted the forward rates (Figure 5c). Such kinetic dependencies suggest that CO_2 and H_2O oxidants (and also their counterparts, CO and H_2) alter the chemical identity and density of active sites and perhaps the C−H bond activation pathway.

DOI: 10.1021/jacs.7b01632
J. Am. Chem. Soc. XXXX, XXX, XXX−XXX

Table 5. Dispersion of Metal Clusters and the Measured Oxygen Contents (O/M_t, Oxygen-to-Total Metal Atoms; O/M_s, Oxygen-to-Surface Metal Atoms) on Co Clusters and Ni-Co Bimetallic Clusters at 873 K

		P_{CO_2}/P_{CO} = 20		P_{CO_2}/P_{CO} = 32		P_{O_2} = 5 kPa
catalyst clusters	dispersion[a] (%)	O/M_t	O/M_s	O/M_t	O/M_s	O/M_t
$12Co/MgO-ZrO_2$	3.5	0.041 ± 0.010	1.10 ± 0.25	0.045 ± 0.010	1.30 ± 0.25	1.03 ± 0.05
$6Ni\text{-}6Co/MgO-ZrO_2$	3.9	0.036 ± 0.010	0.92 ± 0.25	0.039 ± 0.010	0.99 ± 0.25	0.86 ± 0.05

[a]: measured by H_2 uptake at 313 K.

The curious rate dependencies on the CO_2 and CO pressures have led us to explore the thermodynamic connection of CO_2 and CO pressures to the chemical state of Co clusters. The thermodynamically stable state of a cluster is dictated strictly by the oxygen chemical potentials. For Co clusters, the bulk-phase transitions of Co, CoO, and Co_3O_4 are described by the following chemical equations and the associated standard Gibbs free energies,[59] $\Delta G^0_{Co\text{-}CoO}(873\ K)$ and $\Delta G^0_{Co-Co_3O_4}(873\ K)$, respectively, with their values given at 873 K:

$$Co + CO_2 \leftrightarrow CoO + CO,\quad \Delta G^0_{Co\text{-}CoO}(873\ K) = 35\ kJ\ mol^{-1} \tag{7a}$$

$$3Co + 4CO_2 \leftrightarrow Co_3O_4 + 4CO,\quad \Delta G^0_{Co\text{-}Co_3O_4}(873\ K) = 256\ kJ\ mol^{-1} \tag{7b}$$

The standard Gibbs free energy for the bulk-phase transition of Co to CoO at 873 K (eq 7a) is related to the CO_2-to-CO ratio (P_{CO_2}/P_{CO}), according to

$$\Delta G^0_{Co\text{-}CoO}(873\ K) = RT\ \ln\left(\frac{a_{Co}}{a_{CoO}}\frac{P_{CO_2}}{P_{CO}}\right) = RT\ \ln\left(\frac{K_9}{K_7^2K_8K_5K_{10}}\frac{P_{H_2O}}{P_{H_2}}\right) = RT\ \ln\left(\frac{K_{11}^{0.5}}{K_5K_{10}}\left(\frac{P_{O_2(v)}}{P^{\ominus}}\right)^{0.5}\right) \tag{8}$$

where a_{Co} and a_{CoO} denote the thermodynamic activity of solid Co and CoO, respectively, and equal unity for pure phases. The CO_2-to-CO and H_2O-to-H_2 ratios relate to each other via eq 4 and these ratios dictate the oxygen virtual pressures and oxygen coverages, as described in Section 3.1. The Gibbs free energies for bulk CoO and Co_3O_4 formation from Co at 873 K are 35 kJ mol^{-1} (eq 7a) and 256 kJ mol^{-1} (eq 7b), respectively. These values translate to a required CO_2-to-CO ratio of 125 for the bulk oxidation of Co to CoO and 6752 for that to Co_3O_4. These CO_2-to-CO ratios (125 and 6752) are significantly higher than those used in our study (P_{CO_2}/P_{CO} = 0.5–50, P_{H_2O}/P_{H_2} = 0.1–9), an indication that Co clusters must retain their metallic bulk during CH_4–CO_2 catalysis at all relevant conditions, as dictated by the thermodynamics. Previous thermodynamic analysis based on the relative surface energies of Co and CoO has shown that Co clusters retain their metallic bulk at H_2O-to-H_2 ratios below 60 at 700 K.[60] Bulk oxidation of Co clusters must cause concomitant, drastic changes in their surface structures, surface charges (from Co^0 to Co^{2+} for CoO and from Co^0 to a mixture of Co^{2+}-Co^{3+} for Co_3O_4 formation), and in turn the identity of active sites and their functions. In fact, bulk cluster oxidation would increase the first-order rate coefficients markedly by at least 2 orders of magnitude: the first-order rate coefficients on these oxygen-covered metallic surfaces are 0.02 mol (g-atom $Co_{surface}$-s-kPa)$^{-1}$ (Figure 2b) at an O_2 virtual pressure of 1.7×10^{-20} kPa [$P_{O_2(v)}$, attained when the CO_2-to-CO ratio equals 30, $P_{O_2(v)} = K_{CO_2\text{-}O_2}(P_{CO_2}/P_{CO})^2P^{\ominus}$, eq S15, $K_{CO_2\text{-}O_2}$ refers to the equilibrium constant for $2CO_2 \leftrightarrow 2CO + O_2$ reaction, $P^{\ominus}$ refers to the standard atmosphere] versus on the surfaces of bulk oxide (Co_3O_4) of 2.0 mol (g-atom $Co_{surface}$-s-kPa)$^{-1}$ at 50 kPa O_2 (actual O_2 pressure, evaluated with CH_4–O_2 mixture, Section S5 of the Supporting Information), when comparing at 873 K. The associated C–H bond activation barrier would decrease commensurately from 148 kJ mol^{-1} (CH_4–CO_2 reactions, Table 3) to 105 kJ mol^{-1} (measured in 1 kPa CH_4 and 50 kPa O_2, 803–973 K, Section S5 of the Supporting Information). Previous studies[41] have reported a similar rate constant increase on Pd, as bulk oxidation transforms the active site-pairs from chemisorbed oxygen pairs (O*-O*) to Pd^{2+}-O^{2-} pairs and the C–H activation transition state from a radical-like [O*···CH_3···OH*]‡ to a more stable four-center [Pd^{2+}···CH_3···H···O^{2-}]‡ structure. In response to these transitions, the C–H activation barrier reduces commensurately from 158 to 61 kJ mol^{-1}. This thermodynamic and kinetic evidence, taken together, suggests that Co clusters remain in their metallic phase during CH_4–CO_2 catalysis.

Despite retaining their metallic bulk, the kinetic responses on Co in Figures 2b and 5 are drastically dissimilar to those expected on Ni and all second- and third-row transition metals (Ru,[3,12] Rh,[3,6–9] Pd,[3,4] Ir,[3,10,11] and Pt[3,5]), on which metal atom pairs catalyze the C–H bond activation. We explore next the possibilities that oxygen adatoms may remain on the surfaces of metallic Co clusters and assist with the C–H bond activation. Oxygen uptake studies (without CH_4) using thermogravimetric methods not only confirm that Co clusters must retain their metallic bulk, but also quantitatively measure the surface oxygen coverage at the CO_2-to-CO ratios and oxygen virtual pressures ($P_{O_2(v)}$) relevant to CH_4–CO_2 reactions. As shown in Table 5, exposure of the Co clusters to a 20 CO_2:1 CO mixture at 873 K leads to an O/Co_t ratio (oxygen-to-total Co-atoms) of 0.041 ± 0.010, which corresponds to O/Co_s ratio (oxygen-to-surface Co-atoms) of 1.10 ± 0.25. At a higher CO_2-to-CO ratio of 32, the O/Co_t ratio increases to 0.045 ± 0.010 and the related O/Co_s ratio to 1.30 ± 0.25. These O/Co_t and O/Co_s values confirm that cluster surfaces are covered with reactive O* species. In a separate controlled experiment, exposing the Co clusters to 5 kPa O_2 (873 K, 4 h) leads to an O/Co_t ratio of 1.03 ± 0.05, which confirms the complete bulk oxidation of Co to CoO. Titration of carbon-containing debris (CH_x*, x = 0–4) with oxygen shows that the carbon coverages (CH_x*/Co_s) were below the detection limit (<0.05 ± 0.05) in a 20 CO_2:1 CO mixture or during CH_4–CO_2 reactions (5–20 kPa CH_4–

DOI: 10.1021/jacs.7b01632
J. Am. Chem. Soc. XXXX, XXX, XXX–XXX

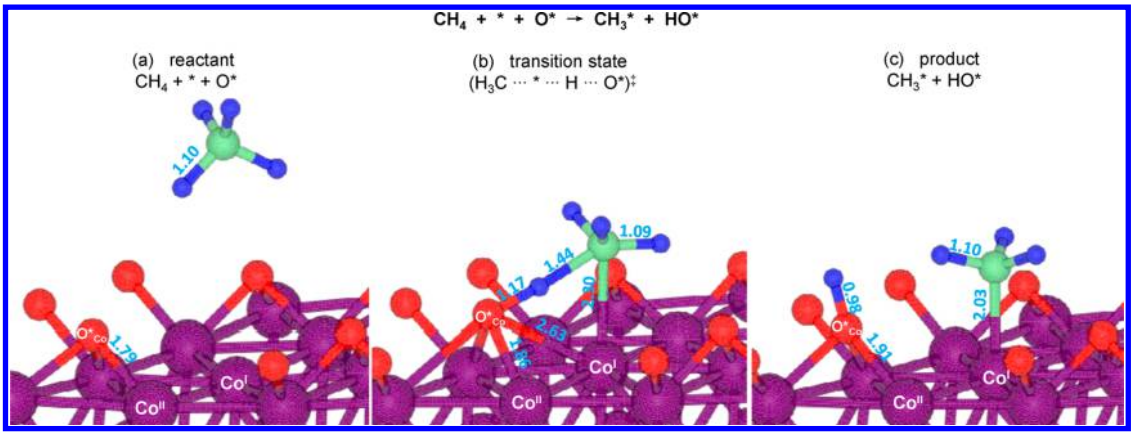

Figure 6. DFT-calculated structures of reactant (a), transition (b), and product (c) states for C−H bond activation step on Co metal (Co^{I}) and oxygen adatom (O^*_{Co}) site-pairs ($*\text{-}O^*_{Co}$) at 0.75 ML O*-covered Co(111) surface ($E_{a,*\text{-}O^*_{Co}}$ = 172 kJ mol^{-1}, ΔH_{rxn} = 110 kJ mol^{-1}; energy changes with respect to the energy of gas-phase CH_4; bond distance unit in Å).

10 kPa CO_2, Figure 4) at 873 K. Thus, Co clusters remain free of CH_x* species.

The kinetic dependencies (Figures 2b and 5), RWGS equilibration (Figure 2e), CO_2−CO uptakes (Table 5), and oxygen titration on Co clusters (Figure 4), taken together, have provided the clear evidence that oxygen adatoms (O*) are the most abundant surface intermediates and assist with the initial C−H bond activation of CH_4 (Step 1b, Table 1). An O* adatom, together with a vicinal metal site, forms a metal−oxygen site-pair ($*\text{-}O^*_{Co}$) that assists with the kinetically relevant H abstraction from CH_4, forming an adsorbed CH_3* and a chemisorbed OH* species (Step 1b). The involvement of metal−oxygen site-pairs in C−H bond activation is mechanistically analogous to those reported during methane combustion on Pt[42,61] and PdO[41] clusters, ethane combustion on Pt clusters,[61] and dimethyl ether combustion on Pt clusters.[62] The assumption of kinetically irreversible step for C−H bond dissociation on $*\text{-}O^*_{Co}$ site-pairs rather than *-* site-pairs (Step 1b instead of Step 1a) on Co, together with the equilibrated steps for the RWGS reaction (Steps 5 and 7−10), gives the following rate expression for the forward methane turnover on Co clusters ($r_{Co,f}$, derivation in Section S5 of the Supporting Information):

$$r_{Co,f} = \frac{k_{*\text{-}O^*_{Co}} K_5 K_{10} P_{CH_4} \frac{P_{CO_2}}{P_{CO}}}{\left(1 + K_5 K_{10} \frac{P_{CO_2}}{P_{CO}}\right)^2} = \frac{k_{*\text{-}O^*_{Co}} \frac{K_9}{K_7^2 K_8} P_{CH_4} \frac{P_{H_2O}}{P_{H_2}}}{\left(1 + \frac{K_9}{K_7^2 K_8} \frac{P_{H_2O}}{P_{H_2}}\right)^2} \quad (9)$$

$$[*] \quad [O^*] \qquad [*] \quad [O^*]$$

where $k_{*\text{-}O^*_{Co}}$ is the rate constant for C−H bond activation on a Co- and O-atom site-pair ($*\text{-}O^*_{Co}$, Step 1b), and K_5K_{10} and $K_9/K_7^2K_8$ are the products of equilibrium constants defined in Table 1. Rearranging eq 9 leads to a first-order rate coefficient ($k^{1st}_{Co,f}$) that depends strictly on the operating CO_2-to-CO or H_2O-to-H_2 ratios on Co clusters:

$$k^{1st}_{Co,f} = \frac{r_{Co,f}}{P_{CH_4}} = \frac{k_{*\text{-}O^*_{Co}} K_5 K_{10} \frac{P_{CO_2}}{P_{CO}}}{\left(1 + K_5 K_{10} \frac{P_{CO_2}}{P_{CO}}\right)^2} = \frac{k_{*\text{-}O^*_{Co}} \frac{K_9}{K_7^2 K_8} \frac{P_{H_2O}}{P_{H_2}}}{\left(1 + \frac{K_9}{K_7^2 K_8} \frac{P_{H_2O}}{P_{H_2}}\right)^2} \quad (10)$$

Equation 10 accurately describes the observed trends, as shown in Figures 2b and 5, which include both the predicted and measured rate values, and in the parity plot between these rate values in Figure S7. Table 2 shows the resulted $k_{*\text{-}O^*_{Co}}$ and K_5K_{10} values derived from nonlinear regression analyses. Equation 4, together with the equilibrium constants for CO_2−CO interconversion (K_5K_{10}) in Table 2, reflects the O* coverages during steady-state CH_4−CO_2 reactions. The O* coverages increase from 0.60 to 0.96 ML, when the CO_2-to-CO ratio increases from 2 to 30.

A nonlinear regression of the CH_4−CO_2 and CD_4-CO_2 rate data (20 kPa CH_4 or CD_4, 5−25 kPa CO_2, 873 K) in Figure 2b with eq 10 also provides the C−H/C−D kinetic isotope effects, defined here as the elementary rate constant ratio of C−H to C−D activation (KIE = $k_{*\text{-}O^*_{Co}C\text{-}H}/k_{*\text{-}O^*_{Co}C\text{-}D}$) on $*\text{-}O^*_{Co}$ site-pairs. The $k_{*\text{-}O^*_{Co}C\text{-}H}/k_{*\text{-}O^*_{Co}C\text{-}D}$ value is 2.03 ± 0.10 at 873 K (Table 3), much larger than unity, similar to that reported for the C−H bond activation on *-O* site-pairs on Pt clusters in combustion reactions (KIE = 2.05),[42] and much larger than those (KIE = 1.42−1.77) on metal atom site-pairs on Ni,[1] Rh,[9] Pt,[5] Pd,[4] Ir,[11] and Ru[12] clusters in reforming reactions. The strong KIEs reflect a larger difference between the activation free energies of $(H_3C\cdots*\cdots H\cdots O^*)^‡$ and $(D_3C\cdots*\cdots D\cdots O^*)^‡$ activated complexes, which involve an oxygen adatom, than between those of $(H_3C\cdots*\cdots H)^‡$ and $(D_3C\cdots*\cdots D)^‡$ complexes prevalent on metal atom site-pairs. This larger difference reflects a much earlier and stronger interactions of H···O* (and D···O*) than H···* (and D···*) at the transition state, as probed and confirmed next with DFT calculations.

The optimized structures of the reactant, transition state, and product for the initial C−H bond activation of methane catalyzed by a Co-atom and oxygen site-pair ($*\text{-}O^*_{Co}$) on 0.75 ML O*/Co(111) surfaces are shown in Figure 6. O* coverages are held constant at 0.75 ML, consistent with the mechanistic proposal of 0.60 to 0.96 ML required for describing the rate data, with the presence of oxygen vacancies (exposed Co sites), and with oxygen uptake studies (Table 5). At 0.75 ML O*/Co(111), there are two types of O*-atoms [Types (γ) and (δ)], as shown in Figure S9: (i) Type (γ) O-atoms reside at the hcp sites (labeled as A, C, and D) with an O* binding energy of −417 ± 8 kJ mol^{-1} and (ii) Type (δ) O-atoms reside at the hcp sites next to an exposed Co-atom (labeled as B and E) with an O* binding energy of −440 ± 5 kJ mol^{-1}. These O* binding

DOI: 10.1021/jacs.7b01632
J. Am. Chem. Soc. XXXX, XXX, XXX−XXX

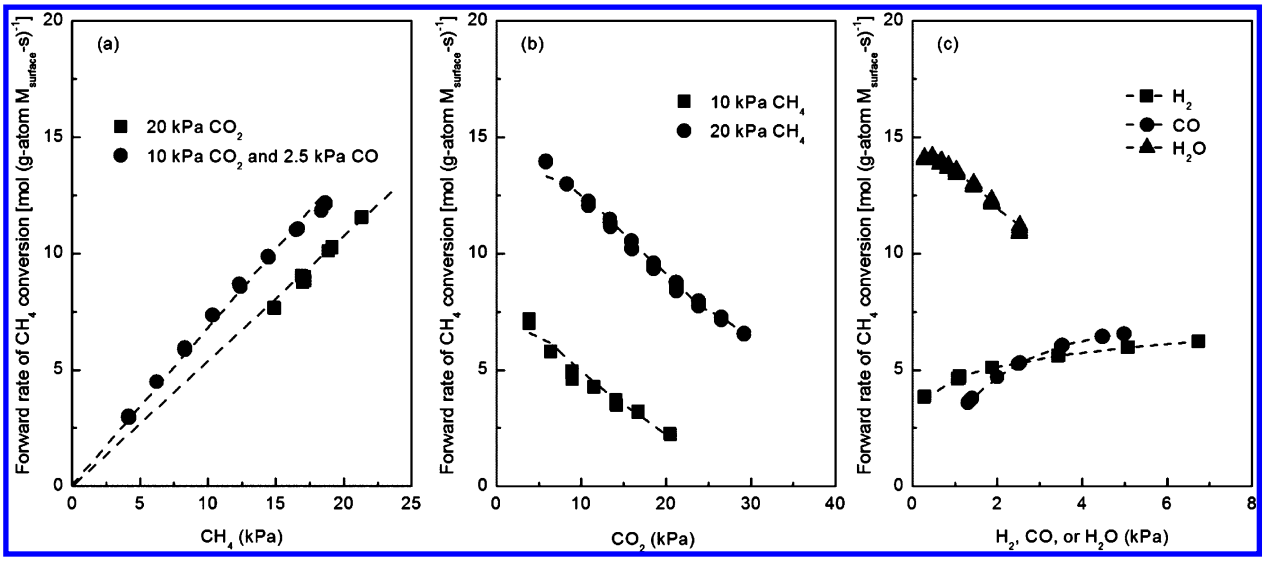

Figure 7. Effects of CH_4 (a), CO_2 (b), and product [(c); 10 kPa CH_4-10 kPa CO_2 with 0.5−10 kPa H_2 (■) or 1.5−6 kPa CO (●); 20 kPa CH_4-3 kPa CO_2 with 0.1−5 kPa H_2O (▲)] partial pressures on the CH_4 forward conversion rate [$r_{Ni\text{-}Co,\delta}$, per total surface Ni- and Co-atoms; (---): predicted CH_4 forward rate from regression of rate data with eq 12] during CH_4−CO_2 reactions at 873 K on 6Ni-6Co/MgO−ZrO_2 (6 g-atom% Ni and 6 g-atom% Co dispersed on MgO−ZrO_2) (2 mg of catalyst, 27 nm mean metal cluster diameter, 10 ZrO_2-to-catalyst intraparticle dilution, and 90 SiO_2-to-catalyst bed dilution; 3.45×10^6 cm^3 g_{cat}^{-1} h^{-1}).

energies on 0.75 ML O*/Co(111) (Table S3) are much less negative than an isolated O* on uncovered Co(111) surfaces of −550 kJ mol^{-1},[58] because lateral repulsive interactions among the co-adsorbed O-atoms weaken the binding strength.

On Co(111) facets covered with 0.75 ML O*, calculations of CH_4 activation were carried out on a site-pair formed from an isolated O* vacancy site (labeled Co^I, Figure 6) and the next nearest O* neighbor. We chose one of the Type (δ) O-atoms (labeled as B and E in Figure S9) as the reactive oxygen site (labeled as O^*_{Co}, Figure 6), because the Type (γ) O-atoms are too far away to interact with the adsorbed CH_4 at the O* vacancy site (Co^I). The C−H bond activation proceeds via a four-center $(H_3C\cdots*\cdots H\cdots O^*)^{\ddagger}$ transition state, during which Co^I inserts into the C−H bond and O^*_{Co} concomitantly abstracts the leaving H. This step resembles the classical σ bond metathesis route with a barrier of 172 kJ mol^{-1} (Table 3). At the transition state, the activated C−H bond elongates slightly from 1.10 to 1.44 Å, much shorter than that of the product state (3.12 Å), consistent with an earlier transition state, and than that of the oxidative addition step on Ni site-pairs in Figure 2g. The Co^I-atom interacts with both the C- and H-atoms, as evidenced from the C−Co^I bond distance of 2.30 Å (vs 2.03 Å in product state, Figure 6) and H−Co^I bond distance of 2.07 Å. The O^*_{Co}, initially adsorbed at the 3-fold hcp site with an O^*_{Co}−Co^{II} bond distance of 1.79 Å, migrates to the bridge position to interact with and stabilize the leaving H-atom (H−O^*_{Co} bond is 1.17 Å at the transition state vs 0.98 Å at the product state).

Bader charge analyses on CH_3, H, and O species (in Table 4) show that the C−H bond activation proceeds via the transfer of H with a proton character, as its charge increases from 0.05 in the CH_4(g) reactant to 0.52 (note: more positive values denote lower electron densities) at the $(H_3C\cdots*\cdots H\cdots O^*)^{\ddagger}$ transition state. At the transition state, the CH_3 fragment acquires a partial negative charge (−0.16 vs −0.10 at the product state), suggesting a direct, heterolytic C−H splitting. Strong repulsive Coulombic interactions between the CH_3 (−0.16) and the O^*_{Co} (−0.88) at the $(H_3C\cdots*\cdots H\cdots O^*)^{\ddagger}$ transition state destabilize the CH_3 fragment; thus, the CH_3 fragment retains most of its gas-phase entropy. These results suggest that the σ bond metathesis pathway on O*-covered Co clusters, despite its lower entropic losses, requires significant enthalpic gains to surmount the transition state. Thus, the σ bond metathesis pathway is much less effective, with a high barrier [172 kJ mol^{-1} on 0.75 ML O*/Co(111) surfaces], than the oxidative addition pathway prevalent on the Ni surfaces [75.4 kJ mol^{-1} on Ni(111), Table 3] and other second- and third-row transition metals [65−70 kJ mol^{-1} on Rh(111),[18,63] 49 kJ mol^{-1} on Ru(1120),[19] 64−80 kJ mol^{-1} on Pd(111),[27,41,63] and 75 kJ mol^{-1} on Pt(111)[27]]. The significant barrier on O*/Co(111) surfaces has made Co an ineffective catalyst for C−H bond activation, despite its ability to retain reactive oxygen species.

3.4. Kinetically Relevant C−H Bond Activation Catalyzed by a Site-Pair Formed from Co-Atom and Vicinal Chemisorbed Oxygen (*-$O^*_{Ni\text{-}Co}$) Prevalent on Bimetallic Ni-Co Clusters. The above findings on Ni and Co monometallic clusters have led us to postulate that C−H bond cleaves effectively on a metal and oxygen site-pair with strong metal-CH_3* and O*-H interactions at the transition state. We recognize that C−H bond activation is most effective on cluster surfaces predominantly covered with reactive oxygen adatoms and (of course) uncovered with carbonaceous deposits (CH_x*), because (i) the lateral interactions between the oxygen adatoms weaken their average binding energies, making them more effective H abstractors and (ii) oxygen adatoms may effectively remove any carbonaceous debris through oxidation reactions. The tuning of the C−H bond pathway begins with incorporating Co into the Ni clusters. Co and Ni preferentially form a miscible alloy at the temperatures relevant for CH_4−CO_2 catalysis, as dictated by thermodynamics.[64]

Figure 7 shows the forward CH_4 turnover rates ($r_{Ni\text{-}Co,\delta}$ per total surface Ni- and Co-atoms) on Ni-Co clusters (27 nm) at 873 K. Ni incorporation and the resulting Ni-Co alloy formation lead to rates that are much higher than on monometallic Co clusters while remain a single-value function of the CO_2-to-CO ratio. These rate values are also a lot higher

DOI: 10.1021/jacs.7b01632
J. Am. Chem. Soc. XXXX, XXX, XXX−XXX

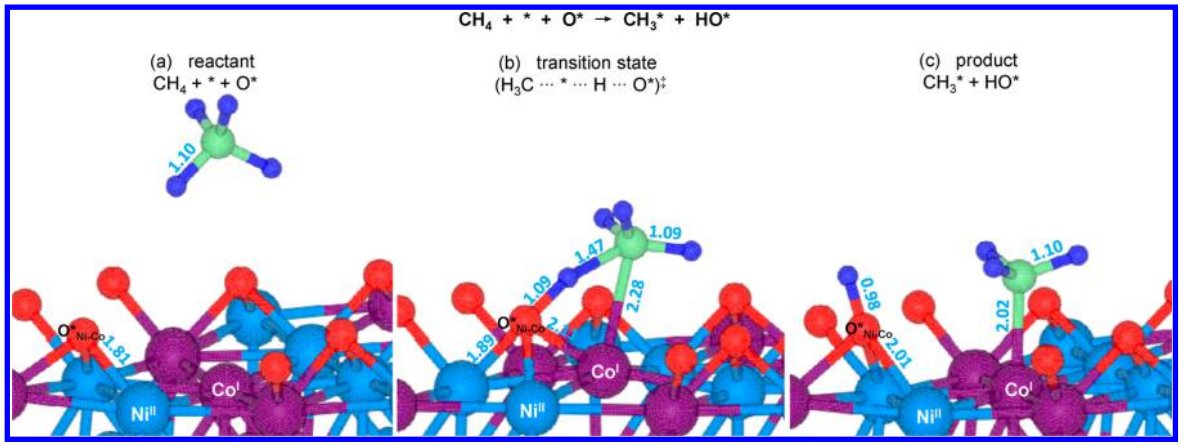

Figure 8. DFT-calculated structures of reactant (a), transition (b), and product (c) states for C−H bond activation step on Co metal (Co^{I}) and oxygen adatom ($O^*_{Ni\text{-}Co}$) site-pairs ($^*\text{-}O^*_{Ni\text{-}Co}$) at 0.75 ML O*-covered Ni-Co(111) surface ($E_{a,^*\text{-}O^*_{Ni\text{-}Co}}$ = 132 kJ mol^{-1}, ΔH_{rxn} = 97 kJ mol^{-1}; energy changes with respect to the energy of gas-phase CH_4; bond distance unit in Å).

than that on monometallic Ni clusters for CO_2-to-CO ratios between 1.1 and 5.0. Specifically, the turnover rates increase linearly with increasing CH_4 pressures (Figure 7a) and depend on both the CO_2-to-CO and H_2O-to-H_2 ratios (Figure 2c). Exposure of the Ni-Co clusters to a 20 CO_2:1 CO mixture at 873 K leads to near monolayer oxygen uptake. The oxygen-to-surface metal ratio, $O/(Ni+Co)_s$, equals 0.92 ± 0.25, which corresponds to the oxygen-to-total metal ratio, $O/(Ni+Co)_t$, of 0.036 ± 0.010 (Table 5). Exposure to a more oxidizing 32 CO_2:1 CO mixture at 873 K further increases the oxygen uptake values to 0.99 ± 0.25 $O/(Ni+Co)_s$ and 0.039 ± 0.010 $O/(Ni+Co)_t$. Such oxygen-to-metal ratios well below the expected stoichiometries for the bulk oxidation of all Co-atoms contained in the Ni-Co clusters to CoO [$O/(Ni+Co)_t$ = 0.5] confirm that Ni-Co clusters retain their metallic bulk.

The rate dependencies (Figures 2c and 7) are consistent with kinetically relevant C−H bond activation catalyzed by Co-atom and chemisorbed oxygen pairs, $^*\text{-}O^*_{Ni\text{-}Co}$, on cluster surfaces predominantly covered with chemisorbed oxygen (O*). This step on $^*\text{-}O^*_{Ni\text{-}Co}$ site-pairs (Step 1b, Table 1), together with quasi-equilibrated dissociation of CO_2 (Steps 5 and 10) or H_2O (Steps 7, 8, and 9), leads to the following expressions for turnover rates ($r_{Ni\text{-}Co,f}$, derived in Section S7 of the Supporting Information) and first-order rate coefficients ($k^{1st}_{Ni\text{-}Co,f}$), with all rate and equilibrium constants defined in Table 1:

$$r_{Ni\text{-}Co,f} = \frac{k_{^*\text{-}O^*_{Ni\text{-}Co}} K_5 K_{10} P_{CH_4} \frac{P_{CO_2}}{P_{CO}}}{\left(1 + K_5 K_{10} \frac{P_{CO_2}}{P_{CO}}\right)^2} = \frac{k_{^*\text{-}O^*_{Ni\text{-}Co}} \frac{K_9}{K_7^2 K_8} P_{CH_4} \frac{P_{H_2O}}{P_{H_2}}}{\left(1 + \frac{K_9}{K_7^2 K_8} \frac{P_{H_2O}}{P_{H_2}}\right)^2} \quad [*] \quad [O^*] \tag{11}$$

$$k^{1st}_{Ni\text{-}Co,f} = \frac{r_{Ni\text{-}Co,f}}{P_{CH_4}} = \frac{k_{^*\text{-}O^*_{Ni\text{-}Co}} K_5 K_{10} \frac{P_{CO_2}}{P_{CO}}}{\left(1 + K_5 K_{10} \frac{P_{CO_2}}{P_{CO}}\right)^2} = \frac{k_{^*\text{-}O^*_{Ni\text{-}Co}} \frac{K_9}{K_7^2 K_8} \frac{P_{H_2O}}{P_{H_2}}}{\left(1 + \frac{K_9}{K_7^2 K_8} \frac{P_{H_2O}}{P_{H_2}}\right)^2} \tag{12}$$

These expressions are identical to those on Co clusters and capture accurately the dependencies shown in Figures 7 and 2c. These expressions also capture the kinetic features at low CO_2-to-CO ratios (1.1−2.0), during which $k^{1st}_{Ni\text{-}Co,f}$ values increase with increasing O* coverages from 0.32 ML to half a monolayer. The positive dependence of $k^{1st}_{Ni\text{-}Co,f}$ is attainable on Ni-Co but not on Co clusters (Figure 2c vs 2b), because this regime corresponds to metal cluster surfaces largely uncovered of reactive oxygen (<0.50 ML O*), unattainable on Co clusters as a result of their much stronger binding to O* than Ni-Co clusters. Nonlinear regression of the rate data in Figures 2c and 7 with eqs 11 and 12 gives $k_{^*\text{-}O^*_{Ni\text{-}Co}}$ and K_5K_{10} values reported in Table 2. Substituting the K_5K_{10} value into eq 4 gives the O* coverages ranging from 0.46 to 0.93 ML as the CO_2-to-CO ratio increases from 2 to 30. C−H/C−D kinetic isotope effects (KIE = $k_{^*\text{-}O^*_{Ni\text{-}Co},C\text{-}H}/k_{^*\text{-}O^*_{Ni\text{-}Co},C\text{-}D}$), defined by the rate constant ratio of C−H bond ($k_{^*\text{-}O^*_{Ni\text{-}Co},C\text{-}H}$) to C−D bond ($k_{^*\text{-}O^*_{Ni\text{-}Co},C\text{-}D}$) activation on these $^*\text{-}O^*_{Ni\text{-}Co}$ site-pairs, are much larger than unity at 873 K (2.15 ± 0.10, in Figure 2c and Table 3). This large KIE is in agreement with those found for C−H bond activation on $^*\text{-}O^*_{Co}$ site-pairs during CH_4−CO_2 reactions on monometallic Co clusters (KIE = 2.05, in Figure 2b and Table 3) and during CH_4−O_2 reactions on Pt clusters (KIE = 2.05).[42]

Next, we probe the pathway of C−H bond activation on Ni-Co(111) surfaces covered with 0.75 ML of oxygen adatoms. Section S6 of the Supporting Information describes the location of the various distinct O* adatoms, their next nearest metal atoms, and their binding energies. There are four types of O*-atoms [Types (ε−θ), Figure S9]: (i) Type (ε) O-atoms reside at Ni-Ni-Co hcp sites (labeled as F, I, and N) with an O* binding energy of −345 ± 8 kJ mol^{-1}, (ii) Type (ζ) O-atoms reside at Ni-Ni-Co hcp sites next to an exposed Co-atom (labeled as G and J) with an O* binding energy of −372 ± 5 kJ

DOI: 10.1021/jacs.7b01632
J. Am. Chem. Soc. XXXX, XXX, XXX−XXX

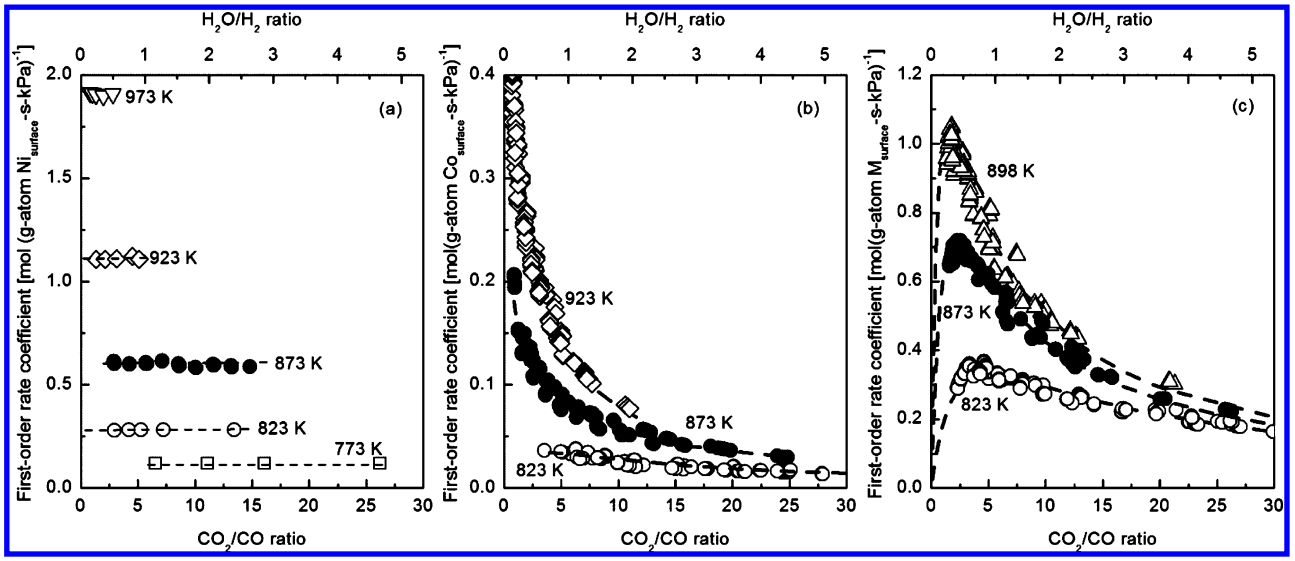

Figure 9. First-order rate coefficients ($k^{1st}_{M,f} = r_{M,f}/P_{CH_4}$, subscript M = Ni, Co, or Ni-Co; $r_{M,f}$ denotes the forward CH_4 conversion rate on metal cluster M) of CH_4 forward conversion, plotted as a function of CO_2-to-CO ratio or H_2O-to-H_2 ratio during CH_4–CO_2 reactions on Ni clusters [(a), 12Ni/MgO–ZrO_2, 26 nm; 10 kPa CH_4 and 4–25 kPa CO_2], Co clusters [(b), 12Co/MgO–ZrO_2, 30 nm; 2–25 kPa CH_4 and 4–25 kPa CO_2], and Ni-Co clusters [(c), 6Ni-6Co/MgO–ZrO_2, 27 nm; 2–25 kPa CH_4 and 4–25 kPa CO_2] at 773–973 K (10 ZrO_2-to-catalyst intraparticle dilution and 90 SiO_2-to-catalyst bed dilution; 4.6×10^5–3.4×10^6 cm^3 g_{cat}^{-1} h^{-1}).

mol^{-1}, (iii) Type (η) O-atoms reside at Co-Co-Ni hcp sites (labeled as H, K, and L) with an O* binding energy of −377 ± 5 kJ mol^{-1}, and (iv) Type (θ) O-atoms reside at Co-Co-Ni hcp sites next to an exposed Ni-atom (labeled as M and O) with an O* binding energy of −416 ± 5 kJ mol^{-1}. Calculations of CH_4 activation were carried out on a site-pair formed from an exposed metal site and a vicinal O*-atom. Types (ε) and (η) oxygen (labeled F, H, I, K, L, and N) are too far to interact with the adsorbed CH_4 at the exposed metal sites (Co^I- or Ni^I-atom). In contrast, the Type (ζ) O-atoms (labeled as G and J) next to the exposed Co^I-atom are the most weakly bound [compare to Type (θ) O-atoms (labeled as M and O) next to the exposed Ni^I-atom] and thus are more basic for abstracting the H-atom in CH_4. Therefore, we chose the Co^I site and one of the Type (ζ) oxygen adatoms (G and J) as a metal–oxygen site-pair (*-$O^*_{Ni\text{-}Co}$, labeled as Co^I and $O^*_{Ni\text{-}Co}$, Figure 1c) that cleaves the C–H bond in CH_4.

The exposed Co^I-atom oxidatively inserts into a C–H bond in CH_4 while the vicinal O^*_{Ni-Co} at the Ni-Ni-Co hcp site migrates to the bridge position (Ni–Ni bridge site, Figure 8b) to interact with and then abstract the leaving H-atom. This step involves the formation of a four-centered $(H_3C\cdots*\cdots H\cdots O^*)^{\ddagger}$ transition state, structurally similar to that on 0.75 ML O*-covered Co(111) surfaces (Figure 6), but with a much lower barrier of 132 kJ mol^{-1}. At the transition state, the metal insertion weakens the C–H bond, which elongates from 1.10 Å in the reactant state to 1.47 Å (Figure 8) and stabilizes both the CH_3 fragment (C···Co^I bond distance of 2.28 Å in transition state vs 2.02 Å in product state) and the H-atom (H···Co^I bond distance of 1.85 Å). The exposed Co^I-atom also interacts strongly with $O^*_{Ni\text{-}Co}$ with a $O^*_{Ni\text{-}Co}$···Co bond distance of 2.11 Å to form a more stable four-center transition-state structure and further reduce the C–H bond activation barrier. The bond distance of the activated C–H bond (1.47 Å) is shorter than that on Ni(111) and similar to those on O*-covered Co(111). The O*···H bond is almost fully formed with a bond distance of 1.09 Å (vs 0.98 Å at the product state).

Bader charge of the leaving H-atom increases from 0.05 in the CH_4(g) reactant to 0.58 at the $(H_3C\cdots*\cdots H\cdots O^*)^{\ddagger}$ transition state (in Table 4), suggesting that the H leaves as a proton during the C–H bond activation. The attractive Coulombic interactions between the leaving H-atom (0.58) and O^*_{Ni-Co} (−0.99) at the transition state are much stronger on Ni-Co(111) than those on Co(111) surfaces, because of the larger Bader charge differences between the H and O* fragments [Ni-Co(111): 0.58 (H) and −0.99 ($O^*_{Ni\text{-}Co}$) vs Co(111): 0.52 (H) and −0.88 (O^*_{Co})]; thus, the $O^*_{Ni\text{-}Co}$ adatom has a higher affinity toward the leaving H. The Bader charge of the CH_3 fragment varies only slightly along the entire reaction coordinate, i.e., from −0.05 to −0.07; thus, the repulsive Coulombic interactions between the CH_3 (−0.06) and the O^*_{Ni-Co} (−0.99) remain insignificant. These results suggest that the σ bond metathesis pathway of C–H bond activation on O*-covered Ni-Co clusters is much more effective and with a barrier of 132 kJ mol^{-1} on 0.75 ML O*/Ni-Co(111) surfaces than that of 172 kJ mol^{-1} on 0.75 ML O*/Co(111) surfaces.

3.5. Distinct Activation Barriers and Entropies Required for the Various C–H Bond Activation Routes Catalyzed by Metal Atom Site-Pairs (*-*) on Ni Clusters and Metal–Oxygen Site-Pairs (*-O^*_{Co} or *-$O^*_{Ni\text{-}Co}$) on Co and Ni-Co Clusters.

We compare next the measured and calculated C–H bond activation enthalpies ($\Delta H_i^{\ddagger}$) and entropies ($\Delta S_i^{\ddagger}$) on the three type of active site-pairs i (i = *-*, *-O^*_{Co}, or *-O^*_{Ni-Co}) on Ni, oxygen-covered Co, and oxygen-covered Ni-Co bimetallic clusters. The $\Delta H_i^{\ddagger}$ (or $\Delta S_i^{\ddagger}$) reflects the enthalpy (or entropy) difference between the transition state for C–H bond activation and the CH_4(g). Together, they give the activation free energies ($\Delta G_i^{\ddagger}$) within the framework of transition-state theory and in turn the rate constant for C–H bond activation, according to

DOI: 10.1021/jacs.7b01632
J. Am. Chem. Soc. XXXX, XXX, XXX–XXX

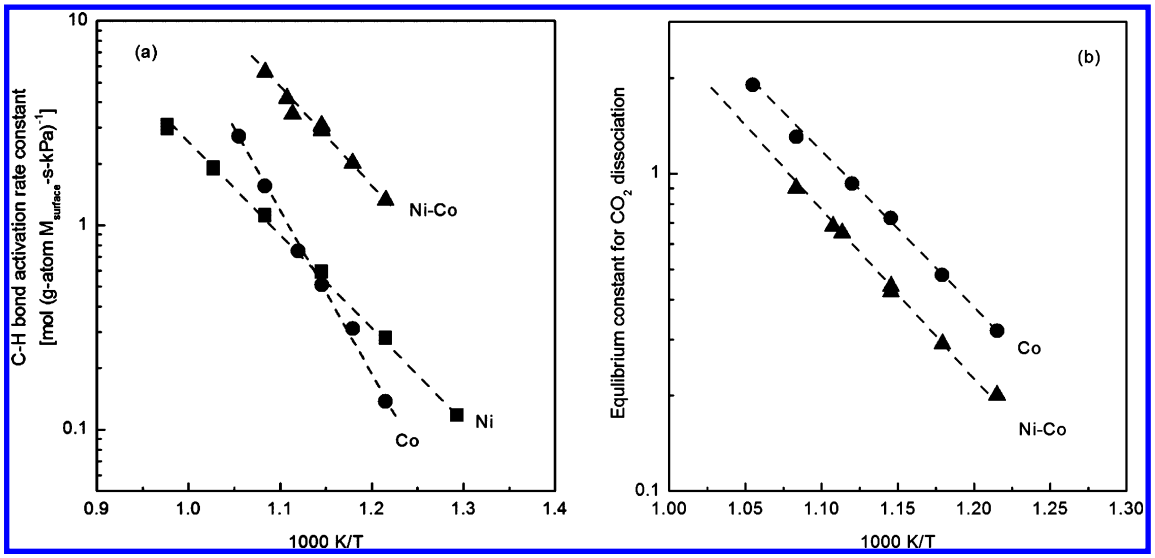

Figure 10. Temperature dependence of the elementary C−H bond activation rate constants [$k_{*\text{-}*}$ (■) for Ni, $k_{*\text{-}O^*_{Co}}$ (●) for Co, and $k_{*\text{-}O^*_{Ni\text{-}Co}}$ (▲) for Ni-Co; in Table 1] on Ni, O*-covered Co, and O*-covered Ni-Co bimetallic clusters (a) and equilibrium constants of CO_2 dissociation to CO and chemisorbed O* ($CO_2(g)+* \leftrightarrow CO(g)+O^*$, eq 14) [$K_{CO_2\text{-}CO,*\text{-}O^*_{Co}}$ (●) for Co and $K_{CO_2\text{-}CO,*\text{-}O^*_{Ni\text{-}Co}}$ (▲) for Ni-Co] on O*-covered Co and O*-covered Ni-Co clusters (b) [Ni clusters, 12Ni/MgO−ZrO_2, 26 nm; Co clusters, 12Co/MgO−ZrO_2, 30 nm; Ni-Co bimetallic clusters, 6Ni-6Co/MgO−ZrO_2, 27 nm; 10 ZrO_2-to-catalyst intraparticle dilution and 90 SiO_2-to-catalyst bed dilution; 4.60×10^5−3.45×10^6 cm^3 g_{cat}^{-1} h^{-1}].

$$k_i = \frac{k_B T}{h} \exp\left(-\frac{\Delta G_i^{\ddagger}}{k_B T}\right) = \frac{k_B T}{h} \exp\left(\frac{\Delta S_i^{\ddagger}}{k_B}\right) \exp\left(-\frac{\Delta H_i^{\ddagger}}{k_B T}\right) \quad (13)$$

where k_B and h denote the Boltzmann and Planck constants, respectively. Regression of the rate data in Figures 2 and 9, measured between 773 and 973 K and 2−25 kPa CH_4, 4−30 kPa CO_2, and 0.7−6 kPa CO, which correspond to CO_2-to-CO ratios within the range of 0.5−50, gives the respective rate constants for C−H bond activation (k_i, i = *-*, *-O^*_{Co}, or *-$O^*_{Ni\text{-}Co}$) on Ni, Co, and Ni-Co bimetallic clusters, are shown as a function of inverse temperature in Figure 10a. Within this temperature range, rate dependencies for Ni, Co, and Ni-Co bimetallic clusters are identical to their respective dependencies reported in Figure 9, an indication that the kinetically relevant step and identity of most abundant surface intermediates for each metal remain unchanged.

The Arrhenius dependencies for C−H bond activation rate constants on Ni ($k_{*\text{-}*}$, eq 5), Co ($k_{*\text{-}O^*_{Co}}$, eq 10), and Ni-Co bimetallic ($k_{*\text{-}O^*_{Ni\text{-}Co}}$, eq 12) clusters are shown in Figure 10a and the measured barriers ($E_{a,i}$) and activation entropies ($\Delta S_i^{\ddagger}$) are summarized in Table 3 together with DFT-calculated barriers ($E_{a,cal,i}$, subscript "cal" denotes DFT calculated value). The measured activation energies for C−H bond activation on *-* site-pair ($E_{a,*\text{-}*}$) are 85 ± 5 kJ mol^{-1}. DFT calculations show that C−H bond lengthens as Ni surfaces donate the electron density into the C−H antibonding orbital (σ_{C-H}*) in an incipient Ni insertion step that forms the three-center $(H_3C\cdots*\cdots H)^{\ddagger}$ transition state (Figure 2g). Thus, the barrier (75 kJ mol^{-1}, Table 3) relates closely to the extent of interactions between the CH_3 fragment and the Ni-atom at the transition state. This process closely resembles the oxidative addition pathway of methane catalyzed by noble metal surfaces [64−73 kJ mol^{-1} on Pd(111)[41,63] and 65−70 kJ mol^{-1} on Rh(111)[18,63]] and by organometallic complexes (95 kJ mol^{-1} on Pt^{II}-NHC[22] and 87 kJ mol^{-1} on Pd^0-NHC[23]). Activation entropies are significantly negative on Ni clusters (−112 J mol^{-1} K^{-1}), because the surface Ni-atom interacts and stabilizes CH_3 fragments at the transition state.

In contrast, C−H bond activation barriers on *-O^*_{Co} site-pairs on O*-covered Co clusters ($E_{a,*\text{-}O^*_{Co}}$) are much higher (experiment: 148 kJ mol^{-1}, DFT calculated: 172 kJ mol^{-1} on 0.75 ML O*/Co(111), Table 3) than those on the Ni-atom pairs. The larger barrier is the result of (1) propensity of O* to strongly bind to Co sites [−440 kJ mol^{-1} on 0.75 ML O*/Co(111)] and therefore unable to interact more strongly with the leaving H at the $(H_3C\cdots*\cdots H\cdots O^*)^{\ddagger}$ transition state, (2) the Coulombic repulsion of the electron-rich O* and CH_3 fragment in the transition state weakens the interaction between Co^I and CH_3 fragments, as indicated from the larger $Co^I\cdots CH_3$ bond distance of 2.30 Å versus $Ni^I\cdots CH_3$ bond distance of 2.05 Å, and thus leads to less effective electron donation from the Co surfaces into the C−H antibonding orbital (σ_{C-H}*). This enthalpic penalty is partially compensated by the less negative activation entropies than the oxidative addition step, as the CH_3 fragment is more weakly bound and retains most of its gas-phase entropy at the transition state (Table 3): the activation entropy for the σ bond metathesis step on O*-covered Co clusters ($\Delta S^{\ddagger}_{*\text{-}O^*_{Co}}$) is −41 J mol^{-1} K^{-1} versus that of the oxidative addition step on Ni clusters ($\Delta S^{\ddagger}_{*\text{-}*}$) of −112 J mol^{-1} K^{-1}, respectively.

In contrast, the measured C−H bond activation energy barrier ($E_{a,*\text{-}O^*_{Ni\text{-}Co}}$) on the Co metal and oxygen site-pair (*-$O^*_{Ni\text{-}Co}$) on Ni-Co clusters is much lower than that on Co clusters (95 vs 148 kJ mol^{-1}), as found also with DFT calculations [132 kJ mol^{-1} on 0.75 ML O*/Ni-Co (111) vs 172 kJ mol^{-1} on 0.75 ML O*/Co(111)], as shown in Table 3. The much lower barrier, despite their similar transition-state structures and σ bond metathesis pathways, is in large part a result of the lower oxygen binding energies on Ni-Co than Co clusters. Ni-Co surfaces bind oxygen much more weakly than Co surfaces (−370 kJ mol^{-1} at Ni-Ni-Co hcp sites vs −440 kJ mol^{-1} at Co-Co-Co hcp sites, Table S3). The weakly bound O-atoms retain higher proton affinity and thus interact with the

DOI: 10.1021/jacs.7b01632
J. Am. Chem. Soc. XXXX, XXX, XXX−XXX

leaving H-atoms more strongly at the transition state, thereby reducing the transition-state energy. Previous studies have shown an even lower barrier (94 kJ mol^{-1}), when the oxygen site is even more weakly bound on Pt surfaces [−256 kJ mol^{-1} on 0.67 ML O*/Pt(111)[42]], attainable only when contacting the surfaces to O_2(g) during CH_4−O_2 reactions on Pt clusters (8.5 nm mean Pt cluster).[42] The repulsive Coulombic interactions between the CH_3 (−0.06) and O^*_{Ni-Co} (−0.99) are much weaker on O*/Ni-Co(111) surfaces than those on O*/Co(111) surfaces [−0.16 (CH_3) and −0.88 (O^*_{Co})], thus leading to stronger interactions between Co^I and CH_3 fragments and in turn larger activation entropy losses ($\Delta S^{\ddagger}_{*\text{-}O^*_{Ni\text{-}Co}}$ = −87 ± 10 J mol^{-1} K^{-1}) on O*/Ni-Co(111) than on O*/Co(111) surfaces.

We next compare the measured and predicted reaction enthalpies ($\Delta H_{CO_2-CO,i}$, subscript i = *-O^*_{Co}, or *-O^*_{Ni-Co}) for the CO_2(g)-to-CO(g) interconversion on Co and Ni-Co clusters (combining Steps 5 and 10 in Table 1):

$$CO_2(g) + * \leftrightarrow CO(g) + O^* \quad (14)$$

The reaction enthalpy ($\Delta H_{CO_2\text{-}CO,i}$), together with the reaction entropy ($\Delta S_{CO_2\text{-}CO,i}$), define the Gibbs free energy ($\Delta G_{CO_2\text{-}CO,i}$) and the related equilibrium constant ($K_{CO_2\text{-}CO,i}$ = K_5K_{10}) for the CO_2(g)-to-CO(g) interconversion in eq 14:

$$K_{CO_2\text{-}CO,i} = \exp\left(\frac{-\Delta G_{CO_2\text{-}CO,i}}{RT}\right) = \exp\left(\frac{-\Delta H_{CO_2\text{-}CO,i}}{RT}\right)\exp\left(\frac{\Delta S_{CO_2\text{-}CO,i}}{R}\right) \quad (15)$$

where R denotes the gas constant. The equilibrium constants ($K_{CO_2\text{-}CO,i}$) on Co and Ni-Co clusters, derived from nonlinear regression of the data in Figure 9b,c with the respective eqs (eq 10 or 12), are shown as a function of inverse temperature in Figure 10b. Substituting eq 15 into eq 4 leads to the site ratio of oxygen-to-unoccupied metal on these clusters, [O*]-to-[*], as a function of either the Gibbs free energies ($\Delta G_{CO_2\text{-}CO,i}$) or the related reaction enthalpies ($\Delta H_{CO_2-CO,i}$) and entropies ($\Delta S_{CO_2\text{-}CO,i}$) for the CO_2(g)-to-CO(g) interconversion in eq 14 and the CO_2-to-CO ratios:

$$\frac{[O^*]}{[*]} = K_{CO_2\text{-}CO,i}\frac{P_{CO_2}}{P_{CO}} = \exp\left(\frac{-\Delta G_{CO_2\text{-}CO,i}}{RT}\right)\frac{P_{CO_2}}{P_{CO}} = \exp\left(\frac{-\Delta H_{CO_2\text{-}CO,i}}{RT}\right)\exp\left(\frac{\Delta S_{CO_2\text{-}CO,i}}{R}\right)\frac{P_{CO_2}}{P_{CO}} \quad (16)$$

The reaction enthalpies ($\Delta H_{CO_2-CO,i}$) for CO_2(g) dissociation to CO(g) and O* on metal clusters can be dissected into energies for a sequence of hypothetical steps using a Born−Haber thermochemical cycle construction, in terms of path-independent thermodynamic state functions. These steps include (I) the gaseous CO_2 decomposition to CO(g) and O_2(g) [$CO_2(g) \rightarrow CO(g) + 0.5O_2(g)$, ΔH^0(873 K) = 282 kJ mol^{-1}, eq S13] and (II) the dissociation of dioxygen to chemisorbed oxygen adatoms on 0.75 ML O*-covered metal surfaces [$0.5O_2(g) + * \rightarrow O^*$, $\Delta H_{*\text{-}O^*_{Ni\text{-}Co}}$ = −124.5 kJ mol^{-1} on 0.75 ML O*/Ni-Co(111) and $\Delta H_{*\text{-}O^*_{Co}}$ = −192.5 kJ mol^{-1} on 0.75 ML O*/Co(111), determined by the DFT-calculated O* binding energies and a half of O=O bond energy]. The $\Delta H_{CO_2\text{-}CO,i}$ and $\Delta S_{CO_2\text{-}CO,i}$, determined from the K_5K_{10} ($K_{CO_2\text{-}CO,i}$) values derived from fittings of the rate data in Figure 10b, show that CO_2(g) dissociation to CO(g) and O* (eq 14) on Ni-Co clusters was more endothermic than that on Co clusters. The enthalpy for CO_2(g) dissociation to CO(g) and O* (eq 14), $\Delta H_{CO_2\text{-}CO,i}$, is 100 ± 10 kJ mol^{-1} on Ni-Co clusters versus that of 90 ± 10 kJ mol^{-1} on Co clusters. These results are consistent with those predicted from the Born−Haber thermochemical cycle [$\Delta H_{CO_2\text{-}CO,*\text{-}O^*_{Ni\text{-}Co}}$ = 157.5 kJ mol^{-1} on 0.75 ML O*/Ni-Co (111) vs $\Delta H_{CO_2\text{-}CO,*\text{-}O^*_{Co}}$ = 89.5 kJ mol^{-1} on 0.75 ML O*/Co(111)], because Ni incorporation into Co clusters weakens their average oxygen binding energies (−370 vs −440 kJ mol^{-1}), leading the oxygen coverages on Ni-Co clusters to become lower than that on Co clusters (between 0.46−0.93 ML on Ni-Co and 0.60−0.96 ML on Co, at CO_2-to-CO ratios between 2 and 30). The difference in O* coverages during steady-state reactions on Ni-Co and Co clusters influences their measured enthalpy values, $\Delta H_{CO_2\text{-}CO,i}$. The larger coverages on Co than Ni-Co clusters lead to less exothermic reactions [$CO_2(g) + * \leftrightarrow CO(g) + O^*$, eq 14]; this difference in coverage causes a much smaller enthalpy difference between the Ni-Co and Co clusters derived from experiments than that between the Ni-Co(111) and Co(111), both covered with 0.75 ML O*, from DFT calculations [$(\Delta H_{CO_2\text{-}CO,*\text{-}O^*_{Ni\text{-}Co}} - \Delta H_{CO_2\text{-}CO,*\text{-}O^*_{Co}})_{experiment}$ = 10 kJ mol^{-1} vs $(\Delta H_{CO_2\text{-}CO,*\text{-}O^*_{Ni\text{-}Co}} - \Delta H_{CO_2\text{-}CO,*\text{-}O^*_{Co}})_{theory}$ = 68 kJ mol^{-1}].

4. CONCLUSIONS

Rate measurements and kinetic isotopic studies in the kinetically controlled regime, oxygen uptake/titration experiments, thermodynamic analyses, and density functional theory calculations were used to establish the different C−H bond activation routes and their catalytic requirements during methane dry reforming reactions on Ni and Co monometallic and Ni-Co bimetallic clusters. On these clusters, C−H bond activation in CH_4 is the sole kinetically relevant step for CH_4 activation and the RWGS reaction is chemically equilibrated, irrespective of the metal chemical identity. The active sites involved in the C−H bond activation, however, differ, depending on the oxophilicity of the metal cluster surfaces. On Ni clusters, metal atom sites activate the C−H bond via the oxidative addition route that involves a three-center $(H_3C\cdots*\cdots H)^{\ddagger}$ transition state. Co incorporation onto Ni clusters leads to Ni-Co alloy; it modifies the oxophilicity and transforms the reactive surface intermediates from covering with a small amount of carbonaceous species to nearly saturated with chemisorbed oxygen adatoms. These oxygen adatoms are the most abundant surface intermediates on Ni-Co clusters and on the more oxophilic Co clusters. The oxygen adatoms on Ni-Co clusters, together with vicinal metal sites, form metal−oxygen site-pairs that activate the C−H bond via a σ bond metathesis route through a four-center $(H_3C\cdots*\cdots H\cdots O^*)^{\ddagger}$ transition state with much lower activation free energies than the conventional oxidative addition routes on Ni clusters, because of the smaller, less negative entropy losses required to evolve the transition state, despite the higher activation barrier. This $(H_3C\cdots*\cdots H\cdots O^*)^{\ddagger}$ four-center transition state on Ni-Co clusters is also more stable than that on Co clusters, because of stronger O*−H interactions, leading to lower activation enthalpies and higher

DOI: 10.1021/jacs.7b01632
J. Am. Chem. Soc. XXXX, XXX, XXX−XXX

C−H bond activation rates. The first-order rate coefficients on these oxophilic Co and Ni-Co clusters, acquire a direct dependence on the operating CO_2-to-CO ratios, because these ratios reflect the oxygen chemical potentials and the O* coverages, a condition met when the water−gas shift reaction reaches chemical equilibrium.

■ ASSOCIATED CONTENT

Supporting Information

The Supporting Information is available free of charge on the ACS Publications website at DOI: 10.1021/jacs.7b01632.

Sections S1−S7, providing CH_4 and CO_2 conversion rates after eliminating transport corruptions, thermodynamic constraints, and time-dependent effects during CH_4−CO_2 reactions; derivation of the ratio of chemisorbed oxygen to exposed metal site during CH_4−CO_2 reactions; RWGS approach to equilibrium and derivation of forward rate of CH_4 conversion during CH_4−CO_2 reactions on 12Ni/MgO−ZrO_2, 12Co/MgO−ZrO_2, and 6Ni-6Co/MgO−ZrO_2 catalysts; structures of reactant state, transition state, and product state for the initial C−H bond activation in CH_4 over *-* site-pair on Ni(111) surfaces; and locations and binding energies of O* on Co(111) and Ni-Co(111) facets, including eqs S1−S28, Figures S1−S11, and Tables S1−S3 (PDF)

■ AUTHOR INFORMATION

Corresponding Authors

*chandraveer.singh@utoronto.ca
*cathy.chin@utoronto.ca

ORCID

Chandra Veer Singh: 0000-0002-6644-0178
Ya-Huei Cathy Chin: 0000-0003-3402-4097

Notes

The authors declare no competing financial interest.

■ ACKNOWLEDGMENTS

This study was supported by Natural Sciences and Engineering Research Council of Canada (NSERC) and Canada Foundation for Innovation (CFI). DFT computations were carried out on Compute Canada clusters, SciNet, and Calcul-Quebec consortia. We gratefully acknowledge their support. We acknowledge Drs. Duane Chung and Julian Ross for their scientific input.

■ REFERENCES

(1) Wei, J.; Iglesia, E. *J. Catal.* **2004**, *224*, 370.
(2) Zhang, Z.; Verykios, X. E.; MacDonald, S. M.; Affrossman, S. *J. Phys. Chem.* **1996**, *100*, 744.
(3) Jones, G.; Jakobsen, J. G.; Shim, S. S.; Kleis, J.; Andersson, M. P.; Rossmeisl, J.; Abild-Pedersen, F.; Bligaard, T.; Helveg, S.; Hinnemann, B.; Rostrup-Nielsen, J. R.; Chorkendorff, I.; Sehested, J.; Nørskov, J. K. *J. Catal.* **2008**, *259*, 147.
(4) Yamaguchi, A.; Iglesia, E. *J. Catal.* **2010**, *274*, 52.
(5) Wei, J.; Iglesia, E. *J. Phys. Chem. B* **2004**, *108*, 4094.
(6) Efstathiou, A. M.; Kladi, A.; Tsipouriari, V. A.; Verykios, X. E. *J. Catal.* **1996**, *158*, 64.
(7) Stevens, R. W.; Chuang, S. S. C. *J. Phys. Chem. B* **2004**, *108*, 696.
(8) Múnera, J. F.; Irusta, S.; Cornaglia, L. M.; Lombardo, E. A.; Vargas Cesar, D.; Schmal, M. *J. Catal.* **2007**, *245*, 25.
(9) Wei, J.; Iglesia, E. *J. Catal.* **2004**, *225*, 116.
(10) Wei, J.; Iglesia, E. *Angew. Chem., Int. Ed.* **2004**, *43*, 3685.
(11) Wei, J.; Iglesia, E. *Phys. Chem. Chem. Phys.* **2004**, *6*, 3754.
(12) Wei, J.; Iglesia, E. *J. Phys. Chem. B* **2004**, *108*, 7253.
(13) Liu, H.; Zhang, R.; Yan, R.; Wang, B.; Xie, K. *Appl. Surf. Sci.* **2011**, *257*, 8955.
(14) Zhu, Y.-A.; Chen, D.; Zhou, X.-G.; Yuan, W.-K. *Catal. Today* **2009**, *148*, 260.
(15) Xu, J.; Saeys, M. *J. Phys. Chem. C* **2009**, *113*, 4099.
(16) Nikolla, E.; Schwank, J.; Linic, S. *J. Catal.* **2009**, *263*, 220.
(17) Fan, C.; Zhou, X.-G.; Chen, D.; Cheng, H.-Y.; Zhu, Y.-A. *J. Chem. Phys.* **2011**, *134*, 134704.
(18) Bunnik, B. S.; Kramer, G. J. *J. Catal.* **2006**, *242*, 309.
(19) Ciobica, I. M.; van Santen, R. A. *J. Phys. Chem. B* **2002**, *106*, 6200.
(20) Zuo, Z.; Huang, W.; Han, P.; Li, Z. *Appl. Surf. Sci.* **2010**, *256*, 5929.
(21) Jones, C. J.; Taube, D.; Ziatdinov, V. R.; Periana, R. A.; Nielsen, R. J.; Oxgaard, J.; Goddard, W. A. *Angew. Chem., Int. Ed.* **2004**, *43*, 4626.
(22) Prince, B. M.; Cundari, T. R. *Organometallics* **2012**, *31*, 1042.
(23) Munz, D.; Meyer, D.; Strassner, T. *Organometallics* **2013**, *32*, 3469.
(24) Biswas, B.; Sugimoto, M.; Sakaki, S. *Organometallics* **2000**, *19*, 3895.
(25) Xavier, E. S.; De Almeida, W. B.; da Silva, J. C. S.; Rocha, W. R. *Organometallics* **2005**, *24*, 2262.
(26) Diefenbach, A.; de Jong, G. T.; Bickelhaupt, F. M. *J. Chem. Theory Comput.* **2005**, *1*, 286.
(27) Santen, R. A. v.; Neurock, M.; Shetty, S. G. *Chem. Rev.* **2010**, *110*, 2005.
(28) Xu, J.; Chen, L.; Tan, K. F.; Borgna, A.; Saeys, M. *J. Catal.* **2009**, *261*, 158.
(29) Rostrup-Nielsen, J. R. *J. Catal.* **1984**, *85*, 31.
(30) García-Diéguez, M.; Finocchio, E.; Larrubia, M. Á.; Alemany, L. J.; Busca, G. *J. Catal.* **2010**, *274*, 11.
(31) Nurunnabi, M.; Mukainakano, Y.; Kado, S.; Li, B.; Kunimori, K.; Suzuki, K.; Fujimoto, K.-i.; Tomishige, K. *Appl. Catal., A* **2006**, *299*, 145.
(32) Nikolla, E.; Holewinski, A.; Schwank, J.; Linic, S. *J. Am. Chem. Soc.* **2006**, *128*, 11354.
(33) Zhang, J.; Wang, H.; Dalai, A. K. *J. Catal.* **2007**, *249*, 300.
(34) Huang, Y.; Du, J.; Ling, C.; Zhou, T.; Wang, S. *Catal. Sci. Technol.* **2013**, *3*, 1343.
(35) An, W.; Zeng, X. C.; Turner, C. H. *J. Chem. Phys.* **2009**, *131*, 174702.
(36) Liu, H.; Wang, B.; Fan, M.; Henson, N.; Zhang, Y.; Towler, B. F.; Gordon Harris, H. *Fuel* **2013**, *113*, 712.
(37) Pakhare, D.; Spivey, J. *Chem. Soc. Rev.* **2014**, *43*, 7813.
(38) Theofanidis, S. A.; Galvita, V. V.; Poelman, H.; Marin, G. B. *ACS Catal.* **2015**, *5*, 3028.
(39) Kim, S. M.; Abdala, P. M.; Margossian, T.; Hosseini, D.; Foppa, L.; Armutlulu, A.; van Beek, W.; Comas-Vives, A.; Copéret, C.; Müller, C. *J. Am. Chem. Soc.* **2017**, *139*, 1937.
(40) Takanabe, K.; Nagaoka, K.; Nariai, K.; Aika, K.-i. *J. Catal.* **2005**, *232*, 268.
(41) Chin, Y.-H.; Buda, C.; Neurock, M.; Iglesia, E. *J. Am. Chem. Soc.* **2013**, *135*, 15425.
(42) Chin, Y.-H.; Buda, C.; Neurock, M.; Iglesia, E. *J. Am. Chem. Soc.* **2011**, *133*, 15958.
(43) Lide, D. R. *CRC Handbook of Chemistry and Physics*, 87th ed.; CRC Press: Boca Raton, FL, 2006.
(44) Boudart, M. *Catal. Lett.* **1989**, *3*, 111.
(45) Zhao, X. Q.; Veintemillas-Verdaguer, S.; Bomati-Miguel, O.; Morales, M. P.; Xu, H. B. *Phys. Rev. B: Condens. Matter Mater. Phys.* **2005**, *71*, 024106.
(46) Perdew, J. P.; Burke, K.; Ernzerhof, M. *Phys. Rev. Lett.* **1996**, *77*, 3865.
(47) Blöchl, P. E. *Phys. Rev. B: Condens. Matter Mater. Phys.* **1994**, *50*, 17953.

DOI: 10.1021/jacs.7b01632
J. Am. Chem. Soc. XXXX, XXX, XXX−XXX

(48) Kresse, G.; Joubert, D. *Phys. Rev. B: Condens. Matter Mater. Phys.* **1999**, *59*, 1758.
(49) Monkhorst, H. J.; Pack, J. D. *Phys. Rev. B* **1976**, *13*, 5188.
(50) Henkelman, G.; Uberuaga, B. P.; Jónsson, H. *J. Chem. Phys.* **2000**, *113*, 9901.
(51) Bader, R. F.; MacDougall, P. J. *J. Am. Chem. Soc.* **1985**, *107*, 6788.
(52) Henkelman, G.; Arnaldsson, A.; Jónsson, H. *Comput. Mater. Sci.* **2006**, *36*, 354.
(53) Koros, R. M.; Nowak, E. J. *Chem. Eng. Sci.* **1967**, *22*, 470.
(54) Weiss, B. M.; Iglesia, E. *J. Phys. Chem. C* **2009**, *113*, 13331.
(55) Weiss, B. M.; Iglesia, E. *J. Catal.* **2010**, *272*, 74.
(56) Weiss, B. M.; Artioli, N.; Iglesia, E. *ChemCatChem* **2012**, *4*, 1397.
(57) Blaylock, D. W.; Ogura, T.; Green, W. H.; Beran, G. J. *J. Phys. Chem. C* **2009**, *113*, 4898.
(58) Van Santen, R. A.; Neurock, M. *Molecular heterogeneous catalysis: a conceptual and computational approach*; John Wiley & Sons: New York, 2009.
(59) Chen, M.; Hallstedt, B.; Gauckler, L. J. *J. Phase Equilib.* **2003**, *24*, 212.
(60) van Steen, E.; Claeys, M.; Dry, M. E.; van de Loosdrecht, J.; Viljoen, E. L.; Visagie, J. L. *J. Phys. Chem. B* **2005**, *109*, 3575.
(61) García-Diéguez, M.; Chin, Y.-H.; Iglesia, E. *J. Catal.* **2012**, *285*, 260.
(62) Ishikawa, A.; Neurock, M.; Iglesia, E. *J. Am. Chem. Soc.* **2007**, *129*, 13201.
(63) Liu, Z.-P.; Hu, P. *J. Am. Chem. Soc.* **2003**, *125*, 1958.
(64) Massalski, T. B.; Okamoto, H.; Subramanian, P.; Kacprzak, L.; Scott, W. W. *Binary alloy phase diagrams*; American Society for Metals: Metals Park, OH, 1986; Vol. *1*.

DOI: 10.1021/jacs.7b01632
J. Am. Chem. Soc. XXXX, XXX, XXX−XXX